Cancer Cell

Article

Evolutionary states and trajectories characterized by distinct pathways stratify patients with ovarian high grade serous carcinoma

Graphical abstract

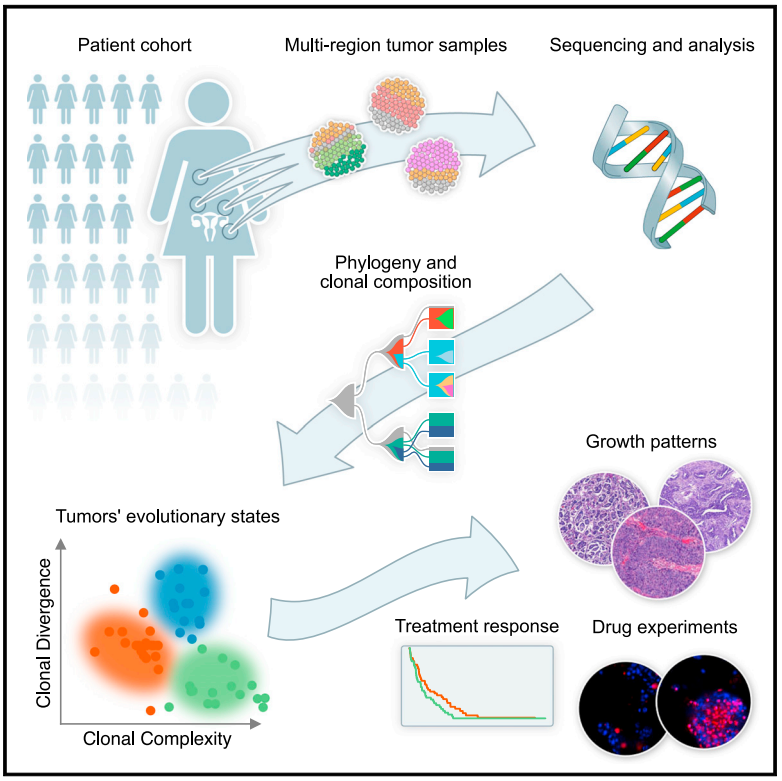

Authors

Alexandra Lahtinen, Kari Lavikka, Anni Virtanen, ..., Johanna Hynninen, Jaana Oikkonen, Sampsa Hautaniemi

Correspondence

jaana.oikkonen@helsinki.fi (J.O.), sampsa.hautaniemi@helsinki.fi (S.H.)

In brief

Lahtinen et al. characterize tumor evolution from 148 patients with high-grade serous carcinoma in the prospective, longitudinal, multiregion DECIDER study. Integration of clonality and clonal divergence reveals three evolutionary states associated with treatment response, pathways, and cell composition. Organoid experiments verify the potential of silencing PI3K/AKT pathway.

Highlights

- Tumor evolution analysis identifies three states with varying clonal heterogeneity
- States are characterized by distinct pathways and associated with treatment response
- Organoid experiments show efficacy of PI3K/AKT pathway inhibition
- Evolutionary states are reflected in the cell composition of the tumor samples

Lahtinen et al., 2023, Cancer Cell *41*, 1103–1117
June 12, 2023
https://doi.org/10.1016/j.ccell.2023.04.017

CellPress

Cancer Cell

CellPress
OPEN ACCESS

Article

Evolutionary states and trajectories characterized by distinct pathways stratify patients with ovarian high grade serous carcinoma

Alexandra Lahtinen,[1] Kari Lavikka,[1] Anni Virtanen,[2] Yilin Li,[1] Sanaz Jamalzadeh,[1] Aikaterini Skorda,[3] Anna Røssberg Lauridsen,[3] Kaiyang Zhang,[1] Giovanni Marchi,[1] Veli-Matti Isoviita,[1] Valeria Ariotta,[1] Oskari Lehtonen,[1] Taru A. Muranen,[1] Kaisa Huhtinen,[1,4] Olli Carpén,[1,2] Sakari Hietanen,[5] Wojciech Senkowski,[6] Tuula Kallunki,[3,7] Antti Häkkinen,[1] Johanna Hynninen,[5] Jaana Oikkonen,[1,8,*] and Sampsa Hautaniemi[1,*]

[1]Research Program in Systems Oncology, Research Programs Unit, Faculty of Medicine, University of Helsinki, 00014 Helsinki, Finland
[2]Department of Pathology, University of Helsinki and HUS Diagnostic Center, Helsinki University Hospital, 00029 Helsinki, Finland
[3]Cancer Invasion and Resistance Group, Danish Cancer Society Research Center, Strandboulevarden 49, 2100 Copenhagen, Denmark
[4]Cancer Research Unit, Institute of Biomedicine and FICAN West Cancer Centre, University of Turku, 20014 Turku, Finland
[5]Department of Obstetrics and Gynaecology, University of Turku and Turku University Hospital, 200521 Turku, Finland
[6]Biotech Research and Innovation Centre, University of Copenhagen, 2200 Copenhagen, Denmark
[7]Department of Drug Design and Pharmacology, Faculty of Health and Medical Sciences, University of Copenhagen, 2200 Copenhagen, Denmark
[8]Lead contact
*Correspondence: jaana.oikkonen@helsinki.fi (J.O.), sampsa.hautaniemi@helsinki.fi (S.H.)
https://doi.org/10.1016/j.ccell.2023.04.017

SUMMARY

Ovarian high-grade serous carcinoma (HGSC) is typically diagnosed at an advanced stage, with multiple genetically heterogeneous clones existing in the tumors long before therapeutic intervention. Herein we integrate clonal composition and topology using whole-genome sequencing data from 510 samples of 148 patients with HGSC in the prospective, longitudinal, multiregion DECIDER study. Our results reveal three evolutionary states, which have distinct features in genomics, pathways, and morphological phenotypes, and significant association with treatment response. Nested pathway analysis suggests two evolutionary trajectories between the states. Experiments with five tumor organoids and three PI3K inhibitors support targeting tumors with enriched PI3K/AKT pathway with alpelisib. Heterogeneity analysis of samples from multiple anatomical sites shows that site-of-origin samples have 70% more unique clones than metastatic tumors or ascites. In conclusion, these analysis and visualization methods enable integrative tumor evolution analysis to identify patient subtypes using data from longitudinal, multiregion cohorts.

INTRODUCTION

High-grade serous carcinoma (HGSC) is the most common epithelial ovarian cancer subtype. HGSC has median latency of more than 10 years[1] and is typically diagnosed at a metastasized state. Accordingly, treatment-naive HGSC tumors have undergone expansions of genomically distinct clones leading to a highly heterogeneous disease[2–5] and already contain drivers for tumor progression and therapy resistance.[6–10] Thus, although 80% of the patients with HGSC respond well to the current standard-of-care, almost all patients experience relapse within a few years after the diagnosis, leading to a five-year survival rate of <40%.[11] We hypothesized that integrating genomic heterogeneity to clonal compositions from phylogenetic analysis will enable stratification of the patients with HGSC into tumor evolutionally defined groups characterized by unique signaling cascades.

Herein, we used data from a prospective, longitudinal, multiregion observational study DECIDER (Multi-Layer Data to Improve Diagnosis, Predict Therapy Resistance and Suggest Targeted Therapies in HGSOC; ClinicalTrials.gov identifier NCT04846933) that started recruitment in 2012. In the DECIDER trial, multiregion samples are collected from consented patients with stage III or IV HGSC and subjected to whole-genome sequencing (WGS) and RNA sequencing (RNA-seq). A goal of DECIDER is to characterize intra- and inter-tumor heterogeneity in patients with HGSC and test whether heterogeneity is associated with treatment response.

We integrated clonal compositions and phylogenetic topologies using WGS data from 510 treatment-naive and post-treatment samples from 148 patients with HGSC to investigate evolutionary states, trajectories, and pathways characterizing them. Fifty-five patients were used as a discovery cohort to define evolutionary states and 93 patients were used as a validation

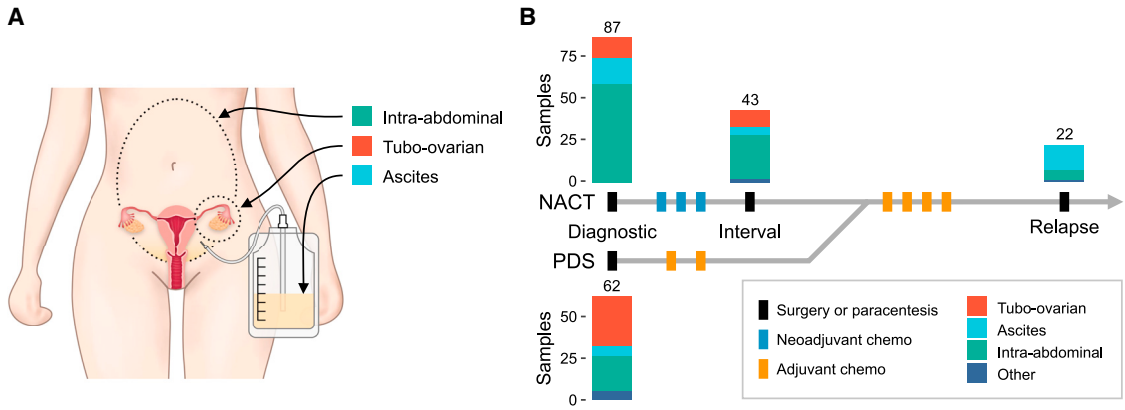

Figure 1. Longitudinal multiregion HGSC cohort enables construction of phylogenetic trees and assessment of clonal compositions at subclonal resolution

(A) Anatomical sites for samples. Intra-abdominal sites include omentum, peritoneum, and bowel mesenterium. Tubo-ovarian sites include fallopian tubes and ovaries. Other metastatic tissue sites include, for example, lymph nodes and liver.

(B) Sample collection at the time of diagnosis (149 samples), at interval surgery (43 samples), and at the time of disease progression (22 samples). PDS, primary debulking surgery; NACT, neoadjuvant chemotherapy.

See also Table S1.

cohort. Transcriptomic data from DNA-matched samples were used to analyze the changes in the pathway activities followed by pre-clinical tumor organoid experiments for validating the key pathway findings. Archived samples collected for routine histopathological diagnostics were used to discover growth pattern differences between the evolutionary states.

RESULTS

Genomic profiling of tumor biopsies in the DECIDER cohort

We prospectively enrolled 55 patients with HGSC and collected 214 samples from tubo-ovarian (ovaries and fallopian tubes) tumors, intra-abdominal metastases (omentum, peritoneum, and bowel mesenterium), other tissues (lymph nodes, liver), and ascites before and after treatments (Figure 1A; Table S1, discovery cohort). The patients were treated according to the HGSC standard-of-care guidelines,[12] i.e., surgery and platinum and taxane combination chemotherapy with angiogenesis and/or poly (ADP-ribose) polymerase (PARP) inhibitors as maintenance therapy (Figure 1B). Archived hematoxylin and eosin (H&E) and immunohistochemical slides were reviewed by a pathologist, to verify histological diagnosis of HGSC for each patient according to the current diagnostic criteria.[13]

Samples were whole-genome sequenced (36× median coverage; range: 24×–96×) and processed in the Anduril bioinformatics workflow platform,[14] as described in STAR Methods. On average, we detected 15,102 mutations per patient (range: 5,451–53,458). Mutational patterns varied in the patients, except for *TP53*, which was mutated in all patients (Table S2). Other significantly mutated genes ($p < 0.001$) after *TP53* were *BRCA2* (11%), *AGAP6* (7%), *MGA* (9%), and *RB1* (5%).

The most frequently amplified copy-number segments at 3q26.2, 3q29, 8q24.21, and 8q24.3 loci were detected in more than half of the patients (Table S3). The top five frequently amplified genes within the COSMIC Cancer Census genes[15] were *MYC* (8q24.21; 36%), *RECQL4* (8q24.3; 31%), *MECOM* (3q26.2; 22%), *CCNE1* (19q12; 22%), and *LYL1* (19p13.13; 18%). The regions deleted in more than half of the patients included 1p36.11, 2q22.1, 3p21.31, 7p22.1, 10q24.32, 11q23.3, 12q24.33, and 14q32.33 (Table S4). The most common COSMIC Cancer Census genes with copy-number loss were *CDH1* (15q21.1; 13%), *FANCA* (16q24.3; 11%), and *CDKN2A* (9p21.3; 11%).

To provide interactive exploration of our cohort, all genomics and key clinical data are available via an interactive visualization tool GenomeSpy (https://csbi.ltdk.helsinki.fi/p/lahtinen_et_al_2023/). GenomeSpy enables rapid navigation of genomic data, and allows filtering, sorting, grouping, and aggregating the samples, as well as bookmarking the most interesting analyses. This enables anyone to rapidly see frequencies of mutations and copy-number variations (CNVs) of any gene or genomic region, as well as their association with platinum-free interval (PFI), whole-genome duplications (WGDs), and other genomic or clinical features. For example, approximately half of HGSC tumors exhibit homologous recombination deficiency (HRD), a predictive biomarker for response to platinum and PARP inhibitors.[16] We quantified HRD-related mutational signatures on the basis of COSMIC version 3.1 single-base substitution (SBS) signatures[17] and included the signatures in the visualization. Furthermore, *CCNE1* is amplified in 15%–20% of patients with HGSC and is predictive of HGSC five-year progression-free survival.[18] The GenomeSpy visualization shows that high *CCNE1* amplifications are associated with low HRD in the DECIDER cohort, supporting the results of Takaya et al.[19]

Phylogenies reveal highly diverse clonal compositions within and between patients with HGSC

Phylogenetic trees and clonal compositions were constructed for 55 patients using somatic mutations adjusted for CNVs (STAR Methods). The DECIDER cohort contains samples from multiple anatomic sites in various time points at the patients' treatment course, which makes visualizing clonal structures challenging

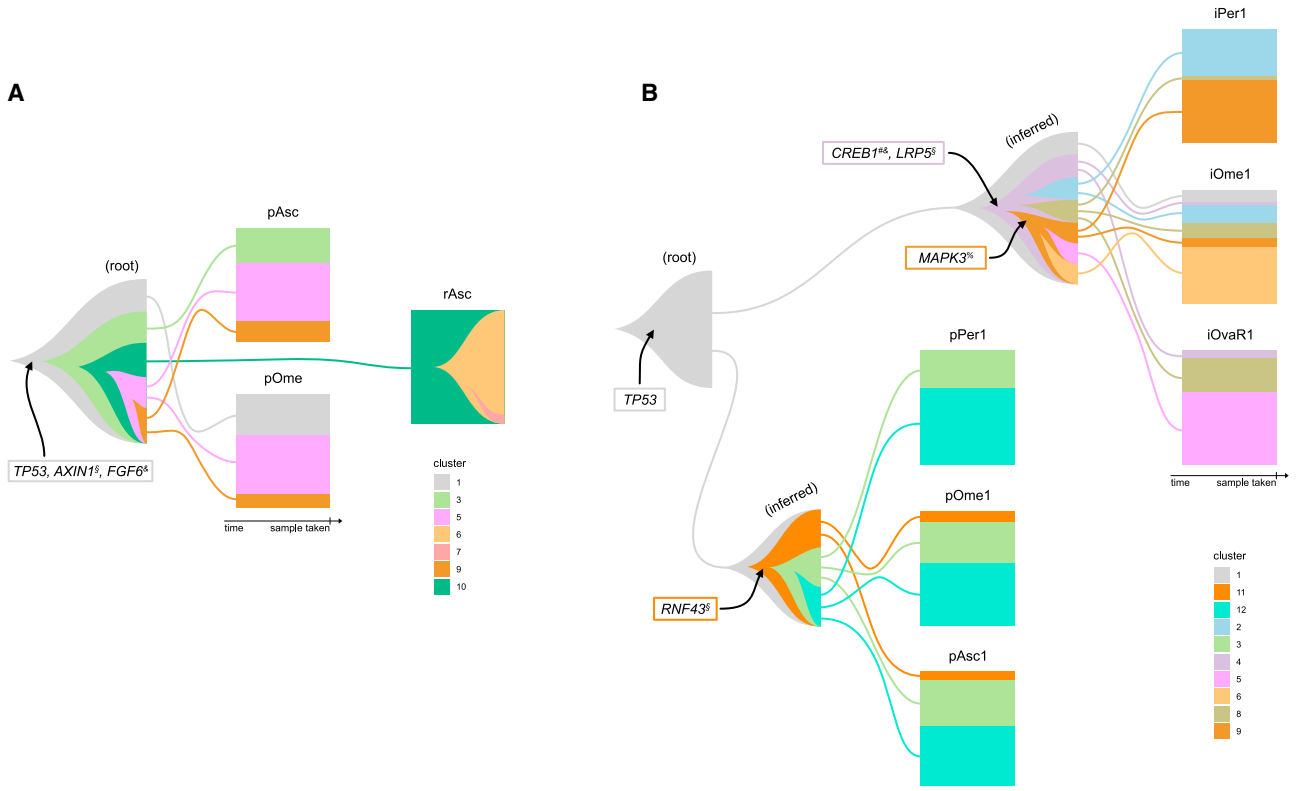

Figure 2. Example jellyfish plots illustrating clonal compositions at various time points

(A) Jellyfish plot of patient EOC742. The rectangular boxes represent ascites and omental samples collected at the time of diagnosis (pAsc and pOme) prior to treatment, and ascites sample at second progression (rAsc), after several months of chemotherapy treatment. The right edge of each box shows the proportion of subclones in the sample. The clonal compositions of the treatment-naive samples obtained from ascites and omentum include two shared subclones 5 and 9, marked as pink and brown boxes, as well as unique subclone 3, marked as light green box in the ascites sample. However, the ascites sample obtained at the second progression reveals a drastically different clonal composition and two sample-specific subclones characterized by the genes *ERCC4* (major clone 6 marked as orange box) and *MYH9* (minor clone 7 marked as red box). Another dominant clone 10, marked as a dark green box, in the relapse sample originated from the same ancestral clone 3 as major clones in the two diagnostic samples. The inferred sample, root, shown on the left, represents a hypothetical sample with subclones that are inherited by multiple real samples. The lines depict the origins of the clones.

(B) Jellyfish plot of patient EOC153 showing drastic subclonal changes in multiple tissues occurring after NACT treatment. Tissue abbreviations: p, primary; i, interval; Per, peritoneum; Ome, omentum; Asc, ascites; OvaR1, right ovary (first sample).

See also Data S1.

with the traditional fishplots.[20] To visualize tumor evolution results from longitudinal and multiregion cohorts, we developed a visualization concept called jellyfish (Data S1). Jellyfish captures the phylogeny of the subclones and enables the comparison of clonal compositions of samples that are acquired from multiple anatomical sites at the same or different time points.

An example of a jellyfish visualization of patient EOC742, who had partial response to the first-line treatment and overall survival (OS) of 38 months, is shown in Figure 2A. The clonal compositions of the diagnostic samples obtained from ascites and omentum include two shared subclones present in almost equal proportions, as well as unique subclones. The ascites sample obtained at the second progression reveals a drastically different clonal composition and two subclones that were not detected in the samples taken earlier during the treatment course and are characterized by somatic mutations in *ERCC4* (major clone) and *MYH9* (minor clone). On the basis of clonal compositions, the dominant clones in the relapse sample originated from the same ancestral clone as major clones in the two diagnostic samples.

Overall, clonal compositions revealed high subclonal heterogeneity in the samples prior to the treatments. In line with earlier studies,[5,21–23] only a small fraction of patients in the DECIDER cohort showed major changes of the clonal structure or genomics landscape before and after the primary treatment (Data S1). A rare example of a complete change in clonal composition affecting multiple tissues can be observed in the jellyfish plot of patient EOC153 (Data S1), who had a complete response to the first-line therapy and OS of 41 months (Figure 2B). The clonal compositions after neoadjuvant chemotherapy (NACT) in all three samples were completely different from the three samples at diagnosis. The clonal compositions of the diagnostic samples were very similar to one another, whereas the NACT-treated samples were very dissimilar to each other.

Tumor heterogeneity is patient and tissue specific

We next quantified heterogeneity at the subclonal level. The two major characteristics of clonal compositions that collectively reflect the heterogeneity measured within and between the

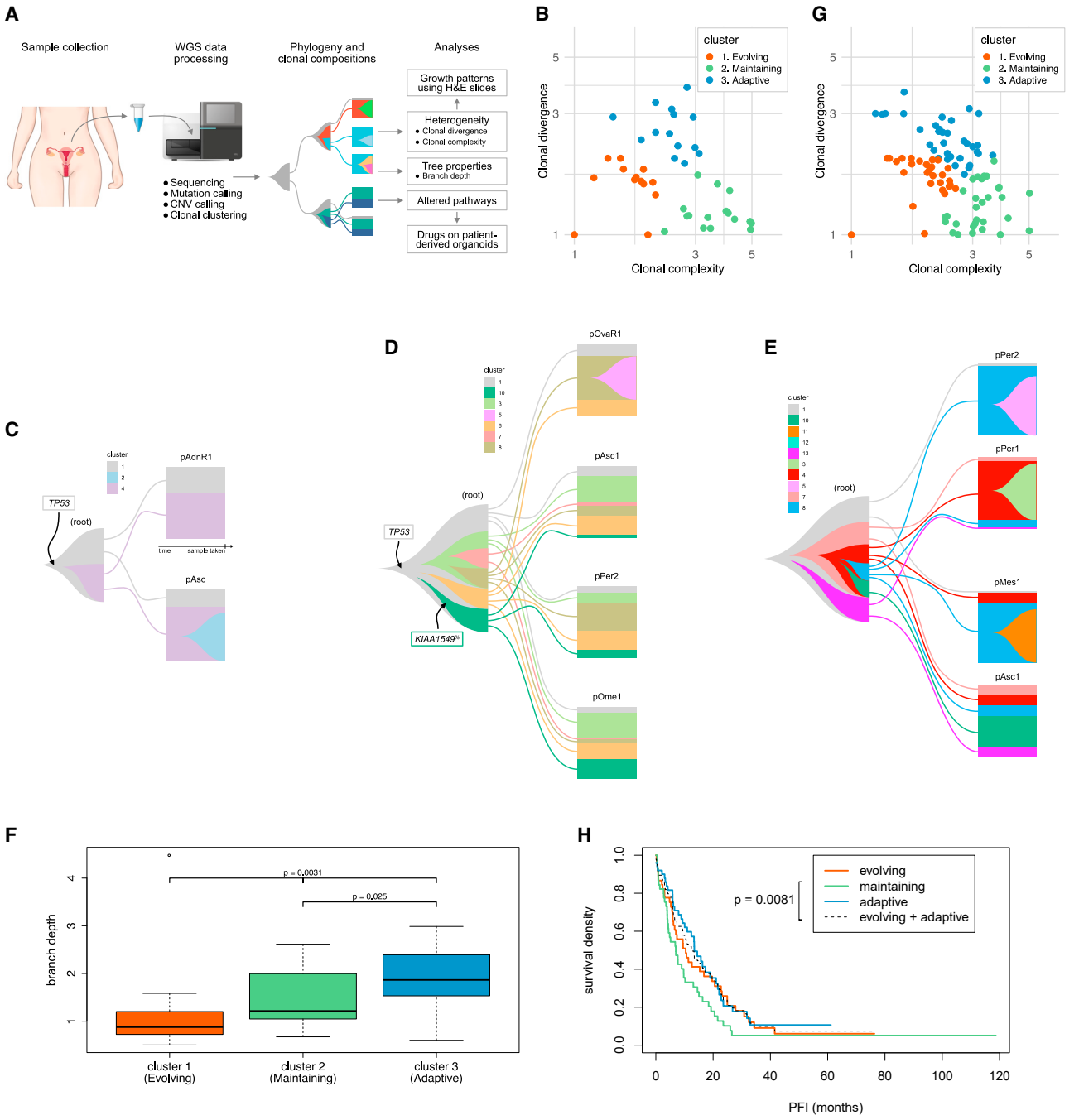

Figure 3. Integration of clonal complexity and divergence enables clustering of patients with HGSC into evolutionary states

(A) The workflow of the study combines three main lines of evolutionary characterization: estimation of evolutionary states on the basis of clonal abundances, temporal order on the basis of the phylogenetic tree topology, and characterization of the underlying biological mechanisms on the basis of pathway aberrations.

(B) The 54 patients (EOC286 was excluded because of the lack of diagnostic samples) clustered (weighted k-means) into three distinct states along clonal complexity (x axis) and clonal divergence (y axis). The placement of each patient in the clustering is available in the corresponding jellyfish plot (Data S1).

(C–E) Jellyfish plots illustrating typical clonal compositions in (C). Cluster 1 (evolving), patient EOC883, (D) cluster 2 (maintaining), patient EOC1129, and (E) cluster 3 (adaptive), patient EOC136. These plots show only diagnostic samples (Table S1); the full plot can be seen in Data S1. Tissue abbreviations: p, primary; AdnR1, adnexa, right; Asc, ascites; OvaR1, ovaries, right; Per, peritoneum; Ome, Omentum; Mes, mesenterium.

(F) Box-and-whisker plots of the branch depths across the three evolutionary states (ANOVA; shown are p values <0.05). Branch depth corresponds to the clonal pseudo-age. Cluster 1 showing the shortest pseudo-age is subsequently referred to as "evolving state." Cluster 2 featuring a stable clonal composition maintained across all samples is referred to as "maintaining state." Cluster 3, distinguished by the unique clonal composition in the samples, is further referred to as "adaptive state."

(legend continued on next page)

samples in a patient are clonal complexity (the number of subclones in the sample) and clonal divergence (the number of unique subclones in the sample). Heterogeneity analyses were carried out in tissue and ascites samples (n = 207).

We first estimated the sample-level clonal complexity, which represents the effective number of clones adjusted for their cellular frequencies (STAR Methods). The sample-level clonal complexity was then averaged to capture the impact of patient and tumor site with ANOVA. Clonal complexity was highly patient specific ($p = 2.1 \times 10^{-6}$) and could not be explained by the anatomical site ($p = 1.5 \times 10^{-3}$), as shown in Table S4. Tubo-ovarian samples exhibited significantly more clonal complexity than the other tissue sites (p = 0.02), such as intra-abdominal metastases and ascites (p = 0.06–0.87).

To quantify sample-level clonal divergence, we first estimated the number of subclones unique to a sample with respect to the global subclone distribution in all samples of the patient. Clonal divergence was averaged to capture and evaluate the impact of patient and tumor site with ANOVA (Table S4). Like clonal complexity, clonal divergence was highly patient-specific ($p = 2.2 \times 10^{-16}$). Interestingly, tubo-ovarian tumors featured 70% more unique clones than the other tumor sites ($p = 5.4 \times 10^{-8}$), whereas ascites samples exhibited 14% less unique clones than the other sites ($p = 6.6 \times 10^{-4}$).

Quantification of tumor heterogeneity enables clustering of patients with HGSC into evolutionary states with a distinctive temporal order

As HGSC tumors exhibited both highly patient-specific clonal complexity and divergence, we sought to identify evolutionary states with similar clonal structure. As neither clonal complexity nor divergence alone produced distinct states (results not shown), we clustered the patients along both quantities (Figure 3A). The 55 patients clustered into three distinct states (Figure 3B; STAR Methods). Cluster 1 consisted of 20 patients and was characterized by a small number of clones (1.79) and high clonal divergence (1.66). An example jellyfish plot of a patient in cluster 1 is illustrated in Figure 3C. Cluster 2 consisted of 16 patients and was characterized by a high number of clones (3.66) and the lowest clonal divergence (1.23). An example jellyfish plot of a patient in cluster 2 (Figure 3D) demonstrates a stable, almost identical clonal composition across all the tissue sites and ascites. Cluster 3 consisted of 18 patients and was characterized by a high number of clones (2.43) and the highest clonal divergence (2.63). An example jellyfish plot of a patient in cluster 3 features an almost unique clonal composition for every sample (Figure 3E).

We tested whether the clonal complexity and divergence were confounded by the number of samples using ANOVA. Clonal complexity and divergence variation explained by clustering were not significantly contributed by the number of samples (complexity, p = 0.70; divergence, p = 0.46). Furthermore, clustering had a significant explanatory power on clonal complexity ($p = 1.5 \times 10^{-12}$) and clonal divergence ($p = 3.6 \times 10^{-10}$) over the number of samples. We also inspected the strength of the clustering and observed that 75% of the patients in the discovery cohort have strong support for their assigned cluster (Bayes factor > 5; Figure S1).

To assess the degree of evolvement or clonal pseudo-age of the three states we used the depth in clonal branches along the topology of the phylogenetic trees (STAR Methods). Cluster 3 featured the highest clonal pseudo-age, followed by cluster 2 and cluster 1 (Figure 3F). The pseudo-ages explained by the clustering were not significantly contributed by the number of samples (p = 0.27), and the clustering had a significant explanatory power over the number of samples (p = 0.04). Accordingly, as cluster 1 exhibited the shortest pseudo-age, it is subsequently referred to as "evolving state." Cluster 2 featured a stable clonal composition maintained across all samples and is referred to as "maintaining state." Cluster 3 was distinguished by the unique clonal composition in the samples and is therefore further referred to as "adaptive state."

Survival analyses reveal maintaining state as the one with poorest clinical outcome

We tested whether the three states have association with the treatment response as measured by PFI and OS. In the discovery set with 55 patients, the survival analysis of maintaining vs. evolving and adaptive states resulted in significant association with PFI (p = 0.04) and similar trend but non-significant association with OS (p = 0.34).

To check whether the PFI and OS associations are reproduced in independent patient samples, we used data from 296 tumor samples from 93 patients with HGSC and identical selection criteria with the discovery cohort from the DECIDER cohort (Table 1; Table S1, validation cohort). The samples were processed in the same way as the discovery cohort samples to acquire phylogenetic trees, clonal compositions, complexity, and divergence (STAR Methods). These 93 patients were mapped to the three states in the clonal complexity and clonal divergence space (Figure 3G). Associations in the validation cohort improved to p = 0.02 (PFI) and p = 0.11 (OS), thereby supporting the associations of the discovery cohort.

To maximize power in the survival analysis we combined the discovery and validation cohorts, which resulted in 148 patients. The numbers of the patients in each state were 49 (evolving), 47 (maintaining), and 52 (adaptive). The clinical and genomic characteristics of the states in the combined cohort are presented as group summaries, along with the corresponding statistical tests in the Figure S1. The Kaplan-Meier plot for the 148 patients with HGSC is shown in Figure 3H. The patients from the maintaining state showed shortest times to relapse, determined by PFI, and the lowest variance, compared with the patients from evolving and adaptive states (p = 0.008). Also in the OS analysis, the patients in the maintaining state have poorest survival (p = 0.047; Figure S2), while

(G) Clustering of 93 patients from the validation cohort into three states along clonal complexity (x axis) and clonal divergence (y axis).
(H) Kaplan-Meier for platinum-free interval (PFI) of 148 patients of the combined cohort from three evolutionary states. In the combined set the association between the three evolutionary states and PFI was statistically significant (p = 0.008).
See also Tables S1–S4, Figures S1 and S2, and Data S1.

Table 1. Basic clinical characteristics of patients in discovery and validation cohorts

	Cohort		
	Discovery	Validation	p value
n	55	93	
Age at diagnosis, y, mean ± SD	68.2 ± 7.5	69.1 ± 9.4	0.43[a]
BMI at diagnosis, kg/m^2, mean ± SD	26.6 ± 5.3	27.2 ± 5.4	0.423[a]
FIGO2014 stage, n (% of row)			0.294[b]
≤IIIA1	0 (0)	4 (100)	
IIIB	1 (33)	2 (67)	
IIIC	34 (34)	64 (65)	
IVA	11 (52)	10 (48)	
IVB	9 (39)	13 (59)	
Treatment strategy, n (% of row)			2.50e-04[b]
PDS	19 (23)	61 (76)	
NACT	36 (51)	32 (47)	
PDS residual tumor, n (% of row)			0.112[b]
0 mm	6 (15)	33 (85)	
1–10 mm	7 (24)	21 (75)	
>10 mm	6 (43)	8 (57)	
IDS residual disease, n (% of row)			0.906[b]
0 mm	12 (60)	8 (40)	
1–10 mm	15 (54)	12 (44)	
>10 mm	4 (57)	2 (33)	
Overall survival, mo, mean ± SD	29.5 ± 13.7	33.0 ± 22.6	0.844[a]
Platinum-free interval, mo, mean ± SD	320.7 ± 274.8	11.07 ± 9.58	0.91[a]

IDS, interval debulking surgery; NACT, neoadjuvant chemotherapy; PDS, primary debulking surgery.
[a]Mann-Whitney U test.
[b]Chi-square test.

the patients from the evolving state demonstrated the best survival odds.

Cell composition differs between evolutionary states and reveals link to tumor morphology

Patients in the maintaining and adaptive states did not differ by their clinical features (Figure S1). However, adaptive group showed enrichment of low ploidy cases without WGD and aneuploidy was more common in the two other states (44% of the patients in the adaptive state had samples without WGD, whereas 21% and 23% of the patients in the maintaining and evolving states, respectively, had samples without WGD). Interestingly, there were no difference in copy-number profiles (https://csbi.ltdk.helsinki.fi/p/lahtinen_et_al_2023/) or significant differences in HRD status among the three states as measured by COSMIC SBS mutational signature 3 (38%, 35%, and 50% signature 3-positive patients in the maintaining, evolving, and adaptive states, respectively).

We next hypothesized that the differences in evolutionary states are reflected in the cell composition, as suggested in earlier studies.[24] To investigate cancer, immune, and stromal components in the treatment-naive samples, we used the PRISM method[25] to decompose RNA-seq data and obtain estimates for the cell compositions (STAR Methods; Table S5). Tumors in the adaptive state were characterized by the highest number of cancer cells and the smallest number of fibroblasts, whereas immune component exhibited equally low numbers in all three states (Figure 4A).

We hypothesized that the cancer/fibroblast ratio reflects the growth pattern of the tumors. To investigate this, we classified morphological growth patterns in omental and tubo-ovarian tumors using 233 scanned H&E-stained slides from 25 patients (STAR Methods; Table S6) and found differences in the growth patterns between high- and low-fibroblast tumors. Firstly, matching to higher purity, the fibroblast-low tumors based on the RNA decomposition often morphologically exhibited predominantly SET (solid, endometrioid, and transitional) and expansive-type papillary growth patterns with minor stromal components. Secondly, fibroblast-high tumors often had destructive-type growth in the form of irregular glandular, nested, and micropapillary structures infiltrating in destructive patterns among ample desmoplastic stromal tissue.

When we stratified the morphological findings by the evolutionary states, we noticed that six of nine patients in the adaptive state had tubo-ovarian tumors with predominantly SET-type growth patterns, and in two patients the pattern was seen also in omental tumors. The SET patterns are often associated with HRD,[26,27] but here they were detected irrespective of HRD status (Table S6). Furthermore, tumors of patients in the evolving state and fibroblast-high composition grew morphologically almost exclusively in a single infiltrative adenopapillary growth pattern (i.e., no additional growth patterns in omental or tubo-ovarian tumors in four of five patients), whereas fibroblast-high tumors from other states often exhibited secondary patterns. Additionally, three of the four tumors that exhibited micropapillary growth pattern were found in the maintaining state (Table S6; Figure 4B).

Evolutionary states are characterized by distinct pathways at genomic and transcriptomic levels

As variation in subclonal heterogeneity may be driven by different biological mechanisms, we studied the subclonal differences in mutated pathways between the evolutionary states using 407 samples from 148 patients. We collected subclonal mutations, annotated them with the genes, and identified enriched biological pathways for each state, as well as pathways shared among the states (Table 2). The significantly enriched cancer pathways common for all states included cell-cell communication, interactions with extracellular matrix, collagen biosynthesis, and receptor tyrosine kinase cascades (Table S7).

The significantly enriched cancer pathways unique to each state comprised MAPK and ERBB2 (evolving state), PI3K/AKT (maintaining state), and NOTCH and WNT (adaptive state) signaling cascades (false discovery rate [FDR]-corrected

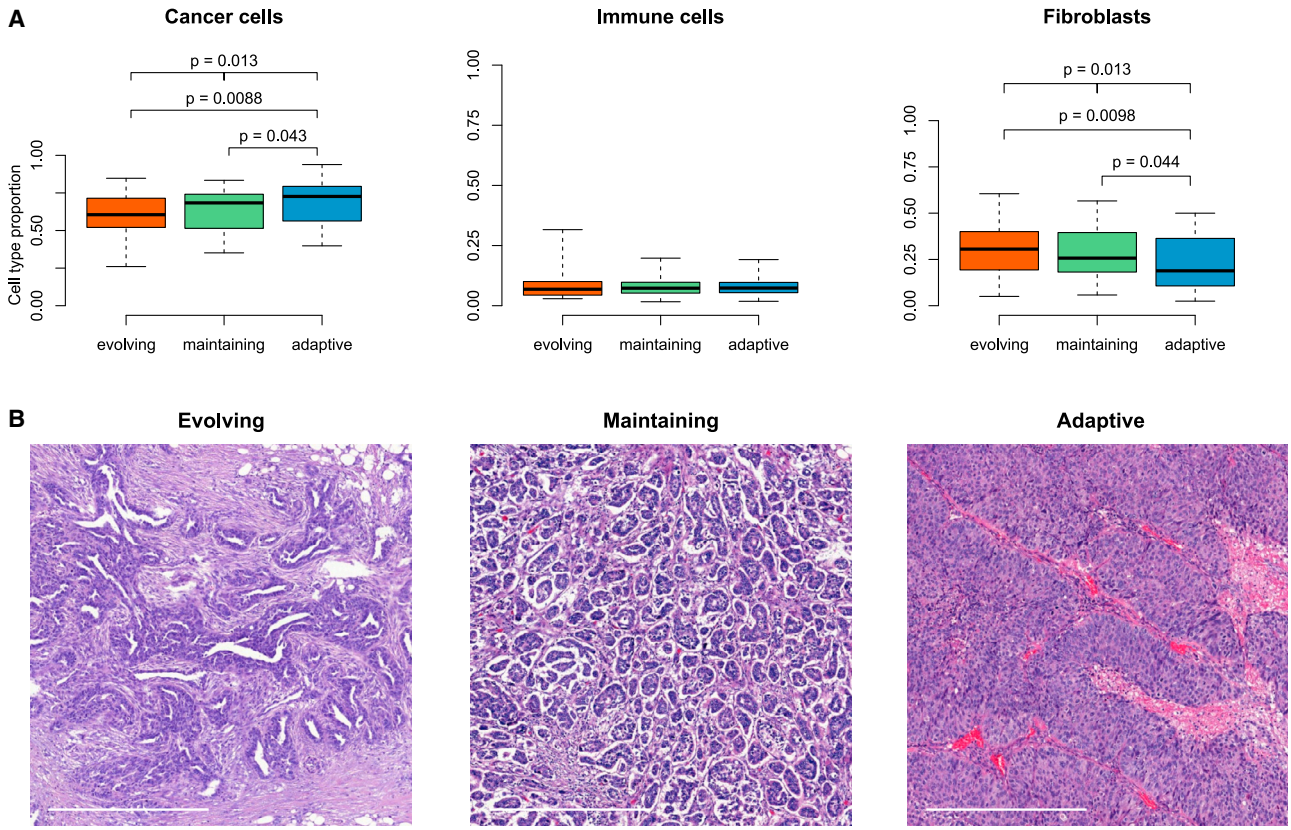

Figure 4. Cell composition varies between evolutionary states, reflecting tumor morphology

(A) Box-and-whisker plots of the cell type abundances across the evolutionary states (ANOVA, adjusted for the tumor sites; shown are p values <0.05; n = 49, 47, and 52 patients, respectively, for evolving, maintaining, and adaptive states). The y axis denotes the sample composition estimated from the bulk RNA decomposition and the whiskers denote range of non-significance at p = 0.05.

(B) Example H&E-stained slides showing characteristic growth pattern found in the tumors occupying evolutionary states: infiltrative adenopapillary in evolving; micropapillary in maintaining; solid, endometrioid, or transitional (SET) growth patterns in adaptive. Scale bar, 500 μm.

See also Tables S5 and S6.

$p < 0.05$). To examine the enrichment of these specific six signaling cascades also at the expression level, we obtained pathway enrichment scores per patient (n = 129) from 317 RNA-seq diagnostic samples matching the WGS samples used in the evolution analyses (STAR Methods; Table S1). Consistent with the genomics findings, NOTCH and WNT signaling cascades were significantly enriched in the adaptive state, and AKT signaling was enriched in the maintaining state (Figure 5A; Table S8).

PI3K/AKT signaling is not affected by chemotherapy and remains enriched at relapse

We assessed the effect of NACT on the evolutionary states using genomics data from 68 samples from 35 patients who were treated with NACT. We found that the evolutionary state remained the same after the chemotherapy in 54% of the patients (Figure S1). Although clonal composition in most cases was stable during the treatment, changes were detected both toward more complex patterns (from evolving and maintaining to adaptive state), as well as toward less complex patterns (from adaptive to maintaining state). Among the changes during NACT, large subclonal changes that could result from strong selection were rare. Examples of these rare subclonal changes are patients EOC153 and EOC26 (Data S1).

We next analyzed the stability of the six enriched signaling cascades after NACT (68 samples from 35 patients) and at relapse (35 relapse samples from 24 patients). Apart from the WNT, all signaling cascades exhibited stability of mutational enrichment after NACT and treatments administered before a relapse. In the tumors from maintaining group, state specific AKT and PI3K signaling remained significantly enriched after NACT and at relapse. In all patients, AKT/PI3K signaling showed significant enrichment also in relapses despite all treatments administered (Figure 5B; Table S9), supporting its key role in tumor progression and chemotherapy resistance.[5,28]

Nested pathway analysis suggests two evolutionary trajectories

We hypothesized that the identified states do not exists independently, but as an evolutionary continuum. Thus, we studied whether the mutational patterns detected between the states are independent or linked via evolutionary trajectories. As evolving state had shortest pseudo-age, we tested whether

Table 2. Unique and common Reactome cancer pathways enriched in the evolutionary states in the combined cohort

Unique driving pathways[a]	Common pathways[b]
Evolving: • Oncogenic MAPK signaling • Signaling by ERBB2 Maintaining: • AKT activation in PI3K/AKT signaling in cancer Adaptive • Signaling by NOTCH • Signaling by WNT in cancer	cell-cell communication extracellular matrix organization • non-integrin membrane-ECM interactions • integrin cell surface interactions • ECM proteoglycans • collagen formation and chain trimerization signaling by receptor tyrosine kinases • PI3K/AKT signaling in cancer • signaling by MET* • signaling by VEGF Rho GTPase cycle MAPK family signaling cascades*

ECM, extracellular matrix.

[a]Listed are unique pathways that were statistically significantly enriched in the state at the threshold of FDR-adjusted $p < 0.05$. We further referred to them as "MAPK" and "ERBB2" in evolving, "AKT" and "PI3K" in maintaining, and "NOTCH" and "WNT" in adaptive states.

[b]Pathways were shared by three states, except for the ones indicated with asterisks, shared by two states.

evolving state could precede the maintaining and adaptive states. To investigate possible transitions occurring from one state to another, we developed a nested pathway analysis approach, which tests the mutational relationships at pathway level between the evolutionary states to estimate the relatedness and identify changed pathways (STAR Methods). On the basis of the nested pathway analysis, we detected links between the states and identified two distinct trajectories characterized by specific pathways (Figure 5C; Figure S3).

The first trajectory suggests that tumors from the patients in the evolving state progress to the maintaining state, driven by changes in PI3K/AKT signaling, CD28 activation, and G2-M transition in the cell cycle pathways. The second step in this trajectory suggests progression to adaptive state, and this transition is marked by the changes in cytokine signaling, MET activating RAS, and VEGF signaling cascade pathways (Table S10).

The second trajectory suggests that tumors occupying evolving state could directly evolve to the adaptive state, bypassing the maintaining state. This trajectory is characterized by the WNT signaling, changes in PTEN regulation, and activation of the cytokine signaling.

Tumor organoid experiments suggest targeting enriched PI3K/AKT pathway with alpelisib

The pathway analyses of the evolutionary states identified highly abundant PI3K/AKT signaling pathway in patients with HGSC. The pathway was enriched in the patients in the maintaining state, which is characterized by poor clinical outcome, and remained enriched after the NACT and at relapse (Figure 5B). Recent studies have shown that targeting PI3K catalytic p110 subunit can lead to anti-tumor effects and potentially assist in overcoming chemoresistance in cancers.[29–31] Accordingly, several clinical approved inhibitors of the pathway exist and are used to treat various cancers.[32,33]

We hypothesized that the PI3K inhibition could be used to target HGSC cells, but mainly in the context of PI3K/AKT pathway-enriched tumors. To test the anti-tumor effect of the PI3K inhibition, we selected five HGSC organoid lines. These lines were established from patient-derived cells at diagnosis, after NACT, or at relapse.[34] Four organoids representing PI3K-pathway-enriched tumors were established from treatment-naive peritoneum sample, NACT-treated omentum sample, and ascites at progression from the patients EOC733 and EOC989. One organoid obtained from treatment-naive omentum sample of EOC1120, which lacked genomic aberration in PI3K/AKT signaling pathway, was used as a control (Figure 6A; Table S11; STAR Methods).

To investigate the possible effect of the PI3K/AKT pathway inhibition in the pre-clinical setting, we exposed organoids to three U.S. Food and Drug Administration (FDA)-approved clinical PI3K inhibitors: alpelisib (a PI3Kα inhibitor approved for treatment of advanced metastatic breast cancer), idelalisib (a PI3Kδ inhibitor approved for treatment of relapsed chronic lymphocytic leukemia), and umbralisib (a PI3Kδ inhibitor whose FDA approval was recently withdrawn). We assessed the drugs by evaluating their effect on cell survival and proliferation, using high-throughput three-dimensional (3D) microscopy (Figure 6A).

After 72 h drug treatment, we measured the tumor cell death within the organoids on the basis of propidium iodide (PI) staining of the DNA of the dead cells (STAR Methods; Figure 6B). We observed significant cytotoxicity with alpelisib and umbralisib in all PI3K/AKT pathway-enriched organoids. Alpelisib showed the strongest and idelalisib the weakest effect on cell viability in all samples (Figure 6C). Matching our hypothesis, the control line (from EOC1120) was completely resistant to idelalisib and umbralisib, and only slightly responsive to the highest concentrations of alpelisib (Figure 6C). We also explored anti-tumor activity of each PI3K inhibitor in terms of proliferation marker Ki67 expression and observed that all three PI3K inhibitors decreased proliferation in all five organoids, except for idelalisib, which did not affect the proliferation of the control organoid line (Figure 6D).

These results support our hypothesis that higher efficacy of the PI3K inhibitors would be achieved for HGSC tumors that were enriched with PI3K aberrations, most observed for the patients in the maintaining state. Overall, the highest cytotoxic efficacy in the PI3K/AKT-enriched organoids was observed for alpelisib, a PI3K p110α-specific inhibitor. Our results indicate that all the examined organoids relied on PI3K/AKT pathway in their proliferation and suggest that the organoids that harbor abundant PI3K/AKT signaling pathway had become dependent, at least to some extent, on the pathway for their survival.

DISCUSSION

We integrated clonal composition and topology of HGSC tumors, discovered three evolutionary states, and estimated the order of their development. Importantly, our stratification of patients into three states prior to treatment enabled us to identify

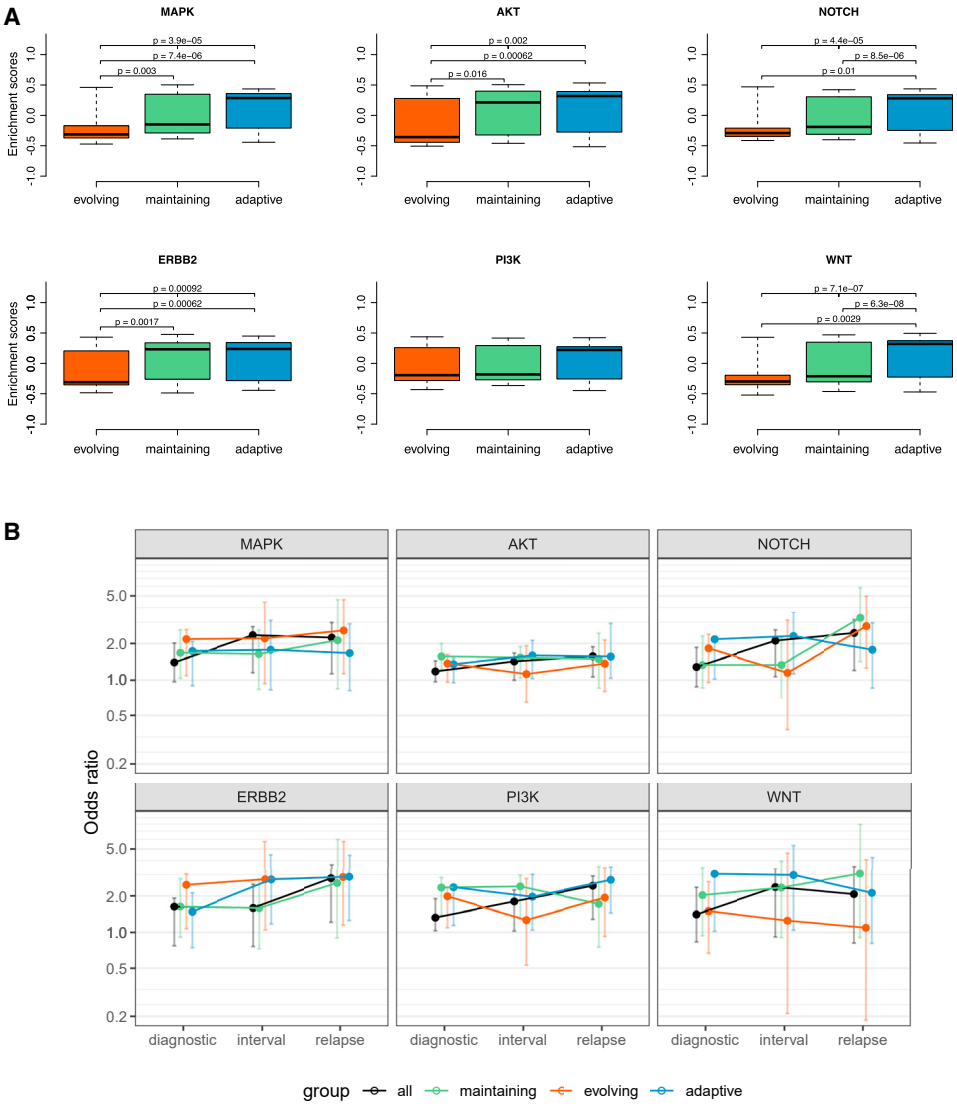

(legend on next page)

a group of patients stratified to the maintaining state and showing shortest time to relapse. The evolutionary states remained stable in most patients after NACT.

The three evolutionary states were characterized by distinct temporal order and enriched aberrations in the oncogenic signaling cascades. The evolving state was estimated to be the youngest state in evolutionary time and showed aberrations in the MAPK and ERBB2 signaling. In evolving state, cancers were most stable and exhibited only few subclones. The evolving state tumors also varied the most between samples and featured more diploid cancers. Patients with tumors in the evolving state have the best response to therapy. The maintaining state, characterized by subclonal aberrations in PI3K/AKT pathway, are suggested to be an intermediate state, where only a fraction of HGSC tumors resides. The maintaining state reflects polyclonal tumors with multiple subclones, whose frequencies remained similar between sites, matching to the previous findings of polyclonal seeding[35] and possible cooperation between subclones.[36] Patients with tumors in the maintaining state are associated with the shortest therapy response, compared with patients with tumors in the evolving or adaptive state. The adaptive state, estimated to be the most evolved among the three evolutionary states, was characterized by various signaling cascades, including driving NOTCH and WNT pathways.

The analysis of tumor composition showed significant differences in tumor/fibroblast ratio between the states, and the morphological subcohort evaluation linked this ratio to morphologically detectable features in the tumors. Furthermore, certain growth patterns seemed to be enriched in the adaptive and maintaining states. In the evolving state, as noted in the analysis of the clonal composition, also morphologically, the fibroblast-high tumors of patients were often homogeneous. These findings suggest that further integration of data describing the tumor phenotype and microenvironment could open paths to clinical integrability of the states.

The nested pathway analysis suggested that the evolutionary states are linked and describe mutational transitions between the states. These evolutionary trajectories suggest that mutational patterns support evolution from evolving state to adaptive either directly or through maintaining state. Patients whose tumors evolve directly to the adaptive state from the evolving state have better survival than patients whose tumors evolve to adaptive state via the maintaining state, the latter characterized by the PI3K/AKT pathway alterations.

We tested whether three PI3K targeting drugs are efficient in tumors with enriched PI3K/AKT pathway using patient-derived tumor organoid lines. All samples proliferated well and used the PI3K/AKT pathway for their proliferation. Interestingly, cell death assay showed that only the organoids with the enriched PI3K/AKT pathway were sensitive to PI3K inhibition, suggesting that they had become dependent on PI3K/AKT pathway for their survival. The most potent effect was observed with the PI3Kα inhibitor alpelisib, which is currently evaluated in EPIK-O phase IIII clinical trial in combination with olaparib in patients with platinum-resistant HGSC.[37] The results from the tumor organoid experiments support the relevance of PI3K/AKT pathway in tumor evolutionary defined subset of patients with HGSC and warrant further investigation with larger numbers of tumor organoids and clinical intervention trials guided by cancer genomics.

As the DECIDER cohort contains samples from several metastatic regions of a patient, we were able to quantify site-specific heterogeneity in HGSC. We found that tubo-ovarian tumors harbor 70% more unique clones than intra-abdominal tumors or ascites, which is in line with the observation that tumor diversity is acquired early in the primary ovarian tumors.[5] Tubo-ovarian samples represent the site-of-origin and early local spreading[4] and have been used extensively in HGSC research, such as in The Cancer Genome Atlas cohort.[38] Given the high number of unique clones in the tubo-ovarian samples, it is possible that the results based on exclusively tubo-ovarian samples are not reproducible in cohorts having samples from other anatomical sites. Another important observation from our heterogeneity analysis is that ascites samples have in general 14% less unique clones than the samples from solid tumors. Thus, cohorts with predominantly ascites samples may present an increased false negative rate.

To provide comprehensive view on our cohort, the genomics data are available via interactive visualization platform GenomeSpy (https://csbi.ltdk.helsinki.fi/p/lahtinen_et_al_2023/). GenomeSpy allows easy and fast exploration of mutations or copy-number aberrations for any gene or genome segment in the human genome in our cohort. In addition to interactive visualization of the genomics data, we developed jellyfish plots that enable visualization of the tumor evolution progress not only longitudinally, but also in spatially different locations.

In summary, our prospective, longitudinal, multiregion study allowed the quantification of tumor evolution from 148 patients with HGSC. Our results stratified the patients on the basis of clonal complexity and divergence to three evolutionary states. The pathways characterizing the states together with organoid experiments suggest specific targets for interventions that have a higher likelihood of being effective in the treatment of patients with relapsed HGSC. Our results underscore the importance of longitudinal multiregion cohorts, such as the DECIDER cohort.

Limitations of the study

The main limitation of this study is that the average WGS coverage for HGSC samples was 36×, which limits resolution

Figure 5. Stability of unique signaling cascades across the treatment and enrichment in RNA-seq data

(A) Box-and-whisker plots of the pathway enrichment scores in RNA expression data across the evolutionary states (ANOVA; shown are p values <0.05; n = 49, 47, and 52 patients, respectively, for evolving, maintaining, and adaptive states). The y axis denotes enrichment scores estimated from the gene set enrichment analysis of the RNA-seq data, and the whiskers denote range of non-significance at p = 0.05.

(B) Enrichment of the unique signaling cascades at diagnosis, interval, and relapse treatment phases. The y axis denotes odd ratios per pathway obtained from the Reactome pathway analysis, and the whiskers denote range of non-significance at p = 0.05 (Fisher's exact test).

(C) Evolutionary trajectory for three states characterized by unique signaling cascades (in nodes) and transition pathways identified by the nested pathway analysis (in clear boxes).

See also Figure S3 and Tables S7, S8, S9, and S10.

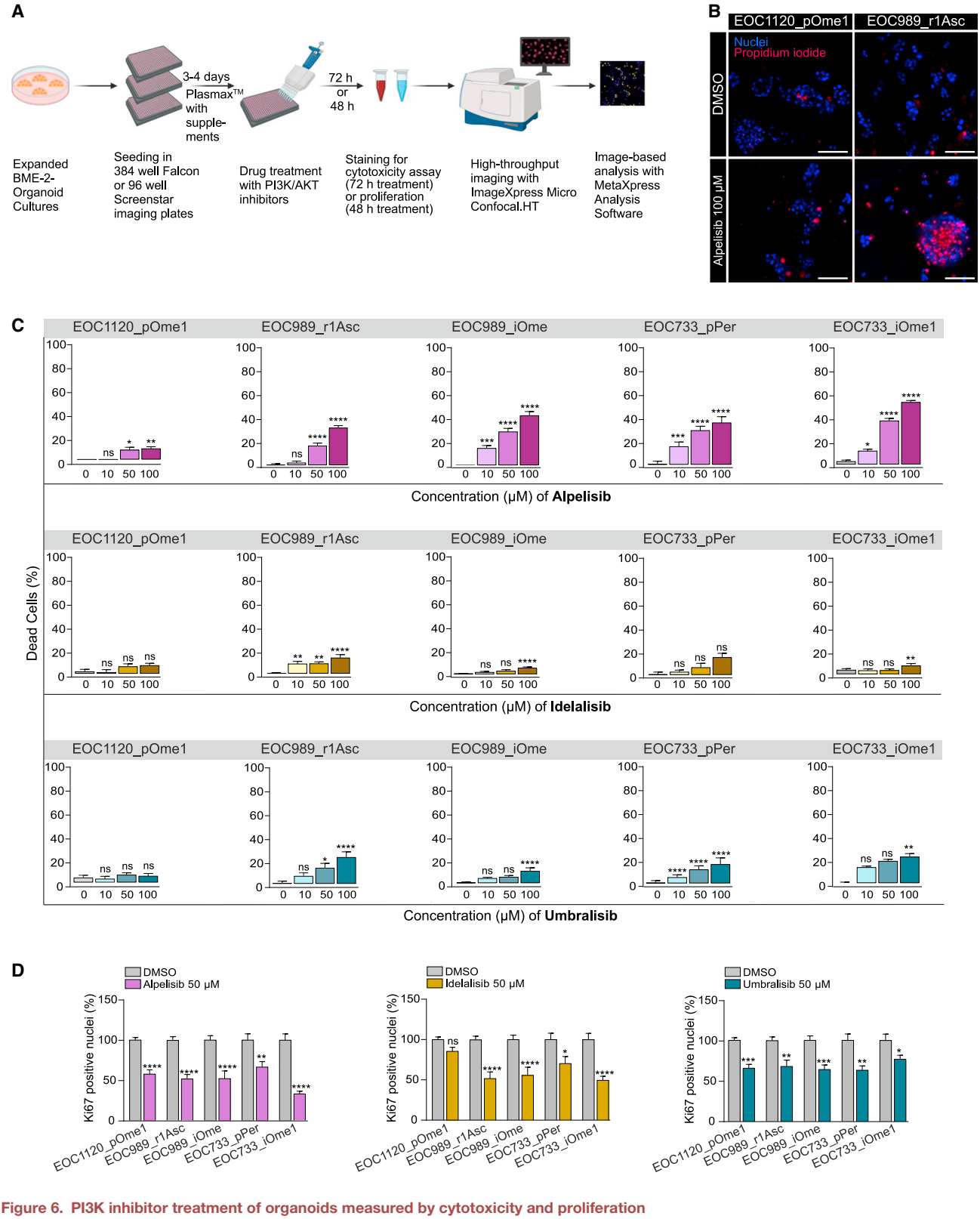

Figure 6. PI3K inhibitor treatment of organoids measured by cytotoxicity and proliferation

(A) Experimental workflow of image-based cell death and proliferation assay on patient-derived organoid cultures using high-throughput confocal microscopy. (B) Representative images of organoids after treatment with DMSO (vehicle control) and alpelisib (100 µM). EOC1120_pOme1 represents the control organoid line with no alteration in the PI3K pathway and EOC989_r1Asc represents an organoid line with enriched PI3K activity. After drug treatment, the total number of nuclei

(legend continued on next page)

to detect rare/small subclones in a sample. As our cohort contains multiple samples from the same patients, we can detect major clones robustly as is evident from agreement of our genomic landscape results with the other HGSC cohorts with a deeper sequencing coverage. The number of samples per patient varied in our cohort, which affects the detection of clusters by PyCloneVI and may cause variability to the state classifications especially on the border of two clusters. The pathway analyses were done with mutation and transcriptomics data, whereas pathways function at protein and phosphorylation level. Thus, our results highlight several pathways that warrant further studies at the protein level.

STAR★METHODS

Detailed methods are provided in the online version of this paper and include the following:

SUPPLEMENTAL INFORMATION

Supplemental information can be found online at https://doi.org/10.1016/j.ccell.2023.04.017.

ACKNOWLEDGMENTS

This project received funding from the European Union's Horizon 2020 Research and Innovation Programme under grant agreements 965193 (DECIDER), 667403 (HERCULES), and 845045 (RESIST3D); the Academy of Finland (projects 325956 and 322927); the Sigrid Jusélius Foundation; Cancer Foundation Finland; and the Danish National Research Foundation (DNRF125). We are grateful to Dr. Ann-Christin Ostwaldt for proofreading the manuscript, Dr. Anna Vähärautio for critical comments on the manuscript, and Prof. Krister Wennerberg for helping with the organoid experiments. The authors wish to acknowledge the CSC-IT Center for Science (Finland) for computational resources.

AUTHOR CONTRIBUTIONS

Conceptualization, A.L., K.L., A.V., T.K., A.H., J.O., and S. Hautaniemi; Methodology and Software, K.L., Y.L., S.J., W.S., and A.H.; Formal Analysis, A.L., K.L., A.V., Y.L., A.S., A.R.L., V.A., O.L., K.Z., S.J., A.H., and J.O.; Investigation, A.L., K.L., A.V., Y.L., A.S., A.R.L., K.H., A.H., J.O., and S. Hautaniemi; Resources, K.L., A.V., Y.L., G.M., S.J., K.Z., V.-M.I., K.H., O.C., S. Hietanen, W.S., T.K., A.H., J.H., and S. Hautaniemi; Data Curation, Y.L., A.V., J.H., T.A.M., J.O., and S. Hautaniemi; Visualization, K.L., A.L., A.V., A.S., A.R.L., A.H., and J.O.; Supervision, T.K., A.H., J.O., and S. Hautaniemi; Project Administration, J.O. and S. Hautaniemi; Funding Acquisition, A.V., O.C., W.S., T.K., A.H., J.H., and S. Hautaniemi; Writing – Original Draft, A.L., J.O., and S. Hautaniemi; Writing – Review & Editing, all authors.

DECLARATION OF INTERESTS

The authors declare no competing interests.

INCLUSION AND DIVERSITY

We support inclusive, diverse, and equitable conduct of research.

Received: August 23, 2022
Revised: February 15, 2023
Accepted: April 25, 2023
Published: May 18, 2023

were stained with Hoechst 33342 (blue) and the dead cells with propidium iodide (PI; red). Images were acquired under 10× magnification with ImageXpress Confocal HT.ai microscope. Scale bar, 50 μm.

(C) Quantification of image-based cell death of organoid lines after 72 h treatment with alpelisib, idelalisib, umbralisib in indicated concentrations (0 as in DMSO vehicle control, 10, 50, and 100 μM) and bortezomib (10 μM, positive control). Cell death is estimated as the percentage of PI-positive cells out of total number of Hoechst 33342-positive nuclei, followed by normalization to the DMSO vehicle control (negative control) and positive control (bortezomib) values. Data are shown as a pool of three biological experiments with four replicates shown as mean ± SEM.

(D) Quantification of image-based cell proliferation of organoids after treatment with 50 μM alpelisib, idelalisib, or umbralisib and DMSO for 48 h. Graphs represent the estimated percentage of Ki67 positive nuclei out of the total number of Hoechst 33852-positive nuclei followed by normalization to the DMSO control values (DMSO values were set as 100% proliferation). Data are shown as a pool of three experiments done as triplicates and presented as mean ± SEM. Statistical significance was calculated using one-way ANOVA combined with Dunnett's multiple comparisons to the negative control. In all cases, $p > 0.05$, $^{*}p < 0.05$, $^{**}p < 0.01$, $^{***}p < 0.001$, and $^{****}p < 0.0001$.

See also Table S11.

REFERENCES

1. Gerstung, M., Jolly, C., Leshchiner, I., Dentro, S.C., Gonzalez, S., Rosebrock, D., Mitchell, T.J., Rubanova, Y., Anur, P., Yu, K., et al. (2020). The evolutionary history of 2,658 cancers. Nature *578*, 122–128. https://doi.org/10.1038/s41586-019-1907-7.
2. Bashashati, A., Ha, G., Tone, A., Ding, J., Prentice, L.M., Roth, A., Rosner, J., Shumansky, K., Kalloger, S., Senz, J., et al. (2013). Distinct evolutionary trajectories of primary high-grade serous ovarian cancers revealed through spatial mutational profiling. J. Pathol. *231*, 21–34. https://doi.org/10.1002/path.4230.
3. Geistlinger, L., Oh, S., Ramos, M., Schiffer, L., LaRue, R.S., Henzler, C.M., Munro, S.A., Daughters, C., Nelson, A.C., Winterhoff, B.J., et al. (2020). Multiomic analysis of subtype evolution and heterogeneity in high-grade serous ovarian carcinoma. Cancer Res. *80*, 4335–4345. https://doi.org/10.1158/0008-5472.CAN-20-0521.
4. Labidi-Galy, S.I., Papp, E., Hallberg, D., Niknafs, N., Adleff, V., Noe, M., Bhattacharya, R., Novak, M., Jones, S., Phallen, J., et al. (2017). High grade serous ovarian carcinomas originate in the fallopian tube. Nat. Commun. *8*, 1093. https://doi.org/10.1038/s41467-017-00962-1.
5. Masoodi, T., Siraj, S., Siraj, A.K., Azam, S., Qadri, Z., Parvathareddy, S.K., Tulbah, A., Al-Dayel, F., AlHusaini, H., AlOmar, O., et al. (2020). Genetic heterogeneity and evolutionary history of high-grade ovarian carcinoma and matched distant metastases. Br. J. Cancer *122*, 1219–1230. https://doi.org/10.1038/s41416-020-0763-4.
6. Castellarin, M., Milne, K., Zeng, T., Tse, K., Mayo, M., Zhao, Y., Webb, J.R., Watson, P.H., Nelson, B.H., and Holt, R.A. (2013). Clonal evolution of high-grade serous ovarian carcinoma from primary to recurrent disease. J. Pathol. *229*, 515–524. https://doi.org/10.1002/path.4105.
7. Kozłowska, E., Färkkilä, A., Vallius, T., Carpén, O., Kemppainen, J., Grénman, S., Lehtonen, R., Hynninen, J., Hietanen, S., and Hautaniemi, S. (2018). Mathematical modeling predicts response to chemotherapy and drug combinations in ovarian cancer. Cancer Res. *78*, 4036–4044. https://doi.org/10.1158/0008-5472.CAN-17-3746.
8. McPherson, A., Roth, A., Laks, E., Masud, T., Bashashati, A., Zhang, A.W., Ha, G., Biele, J., Yap, D., Wan, A., et al. (2016). Divergent modes of clonal spread and intraperitoneal mixing in high-grade serous ovarian cancer. Nat. Genet. *48*, 758–767. https://doi.org/10.1038/ng.3573.
9. Nath, A., Cosgrove, P.A., Mirsafian, H., Christie, E.L., Pflieger, L., Copeland, B., Majumdar, S., Cristea, M.C., Han, E.S., Lee, S.J., et al. (2021). Evolution of core archetypal phenotypes in progressive high grade serous ovarian cancer. Nat. Commun. *12*, 3039–3116. https://doi.org/10.1038/s41467-021-23171-3.
10. Schwarz, R.F., Ng, C.K.Y., Cooke, S.L., Newman, S., Temple, J., Piskorz, A.M., Gale, D., Sayal, K., Murtaza, M., Baldwin, P.J., et al. (2015). Spatial and temporal heterogeneity in high-grade serous ovarian cancer: a phylogenetic analysis. PLoS Med. *12*, 10017899–e1001820. https://doi.org/10.1371/journal.pmed.1001789.
11. Torre, L.A., Trabert, B., DeSantis, C.E., Miller, K.D., Samimi, G., Runowicz, C.D., Gaudet, M.M., Jemal, A., and Siegel, R.L. (2018). Ovarian cancer statistics, 2018. CA A Cancer J. Clin. *68*, 284–296. https://doi.org/10.3322/caac.21456.
12. Colombo, N., Sessa, C., du Bois, A., Ledermann, J., McCluggage, W.G., McNeish, I., Morice, P., Pignata, S., Ray-Coquard, I., Vergote, I., et al. (2019). ESMO–ESGO consensus conference recommendations on ovarian cancer: pathology and molecular biology, early and advanced stages, borderline tumours and recurrent disease. Ann. Oncol. *30*, 672–705. https://doi.org/10.1093/annonc/mdz062.
13. Board, E. (2020). Female genital tumours. In WHO Classification of Tumours (International Agency for Research on Cancer).
14. Cervera, A., Rantanen, V., Ovaska, K., Laakso, M., Nuñez-Fontarnau, J., Alkodsi, A., Casado, J., Facciotto, C., Häkkinen, A., Louhimo, R., et al. (2019). Anduril 2: upgraded large-scale data integration framework. Bioinformatics *35*, 3815–3817. https://doi.org/10.1093/bioinformatics/btz133.
15. Sondka, Z., Bamford, S., Cole, C.G., Ward, S.A., Dunham, I., and Forbes, S.A. (2018). The COSMIC Cancer Gene Census: describing genetic dysfunction across all human cancers. Nat. Rev. Cancer *18*, 696–705. https://doi.org/10.1038/s41568-018-0060-1.
16. Miller, R.E., Leary, A., Scott, C.L., Serra, V., Lord, C.J., Bowtell, D., Chang, D.K., Garsed, D.W., Jonkers, J., Ledermann, J.A., et al. (2020). ESMO recommendations on predictive biomarker testing for homologous recombination deficiency and PARP inhibitor benefit in ovarian cancer. Ann. Oncol. *31*, 1606–1622. https://doi.org/10.1016/j.annonc.2020.08.2102.
17. Alexandrov, L.B., Kim, J., Haradhvala, N.J., Huang, M.N., Tian Ng, A.W., Wu, Y., Boot, A., Covington, K.R., Gordenin, D.A., Bergstrom, E.N., et al. (2020). The repertoire of mutational signatures in human cancer. Nature *578*, 94–101. https://doi.org/10.1038/s41586-020-1943-3.
18. Stronach, E.A., Paul, J., Timms, K.M., Hughes, E., Brown, K., Neff, C., Perry, M., Gutin, A., El-Bahrawy, M., Steel, J.H., et al. (2018). Biomarker assessment of HR deficiency, tumor *BRCA1/2* mutations, and *CCNE1* copy number in ovarian cancer: associations with clinical outcome following platinum monotherapy. Mol. Cancer Res. *16*, 1103–1111. https://doi.org/10.1158/1541-7786.MCR-18-0034.
19. Takaya, H., Nakai, H., Takamatsu, S., Mandai, M., and Matsumura, N. (2020). Homologous recombination deficiency status-based classification of high-grade serous ovarian carcinoma. Sci. Rep. *10*, 2757. https://doi.org/10.1038/s41598-020-59671-3.
20. Miller, C.A., McMichael, J., Dang, H.X., Maher, C.A., Ding, L., Ley, T.J., Mardis, E.R., and Wilson, R.K. (2016). Visualizing tumor evolution with the fishplot package for R. BMC Genom. *17*, 880. https://doi.org/10.1186/s12864-016-3195-z.
21. de Witte, C.J., Kutzera, J., van Hoeck, A., Nguyen, L., Boere, I.A., Jalving, M., Ottevanger, P.B., van Schaik-van de Mheen, C., Stevense, M., Kloosterman, W.P., et al. (2022). Distinct genomic profiles are associated with treatment response and survival in ovarian cancer. Cancers *14*, 1511. https://doi.org/10.3390/cancers14061511.
22. Lee, S., Zhao, L., Rojas, C., Bateman, N.W., Yao, H., Lara, O.D., Celestino, J., Morgan, M.B., Nguyen, T.v., Conrads, K.A., et al. (2020). Molecular analysis of clinically defined subsets of high-grade serous ovarian cancer. Cell Rep. *31*, 107502. https://doi.org/10.1016/j.celrep.2020.03.066.
23. Patch, A.-M., Christie, E.L., Etemadmoghadam, D., Garsed, D.W., George, J., Fereday, S., Nones, K., Cowin, P., Alsop, K., Bailey, P.J., et al. (2015). Whole–genome characterization of chemoresistant ovarian cancer. Nature *521*, 489–494. https://doi.org/10.1038/nature14410.
24. Zhang, A.W., McPherson, A., Milne, K., Kroeger, D.R., Hamilton, P.T., Miranda, A., Funnell, T., Little, N., de Souza, C.P.E., Laan, S., et al. (2018). Interfaces of malignant and immunologic clonal dynamics in ovarian cancer. Cell *173*, 1755–1769.e22. https://doi.org/10.1016/j.cell.2018.03.073.
25. Häkkinen, A., Zhang, K., Alkodsi, A., Andersson, N., Erkan, E.P., Dai, J., Kaipio, K., Lamminen, T., Mansuri, N., Huhtinen, K., et al. (2021). PRISM: recovering cell-type-specific expression profiles from individual composite RNA-seq samples. Bioinformatics *37*, 2882–2888. https://doi.org/10.1093/bioinformatics/btab178.
26. Soslow, R.A., Han, G., Park, K.J., Garg, K., Olvera, N., Spriggs, D.R., Kauff, N.D., and Levine, D.A. (2012). Morphologic patterns associated with BRCA1 and BRCA2 genotype in ovarian carcinoma. Mod. Pathol. *25*, 625–636. https://doi.org/10.1038/modpathol.2011.183.
27. Ritterhouse, L.L., Nowak, J.A., Strickland, K.C., Garcia, E.P., Jia, Y., Lindeman, N.I., Macconaill, L.E., Konstantinopoulos, P.A., Matulonis, U.A., Liu, J., et al. (2016). Morphologic correlates of molecular alterations in extrauterine Müllerian carcinomas. Mod. Pathol. *29*, 893–903. https://doi.org/10.1038/modpathol.2016.82.
28. Liu, R., Chen, Y., Liu, G., Li, C., Song, Y., Cao, Z., Li, W., Hu, J., Lu, C., and Liu, Y. (2020). PI3K/AKT pathway as a key link modulates the multidrug resistance of cancers. Cell Death Dis. *11*, 797. https://doi.org/10.1038/s41419-020-02998-6.
29. Kim, K.-J., Kim, J.-W., Sung, J.H., Suh, K.J., Lee, J.Y., Kim, S.H., Lee, J.-O., Kim, J.W., Kim, Y.J., Kim, J.H., et al. (2020). PI3K-targeting strategy

using alpelisib to enhance the antitumor effect of paclitaxel in human gastric cancer. Sci. Rep. *10*, 12308. https://doi.org/10.1038/s41598-020-68998-w.

30. Konstantinopoulos, P., González-Martín, A., Cruz, F., Friedlander, M., Glasspool, R., Lorusso, D., Marth, C., Monk, B., Kim, J.-W., Alsadius, D., et al. (2021). EPV279/#351 epik-O/ENGOT-OV61: a phase 3, randomized study of alpelisib + olaparib in patients with no germline brca mutation detected, platinum-resistant or -refractory, high-grade serous ovarian cancer. Int. J. Gynecol. Cancer *31*, A139–A140. https://doi.org/10.1136/ijgc-2021-IGCS.350.
31. André, F., Ciruelos, E., Rubovszky, G., Campone, M., Loibl, S., Rugo, H.S., Iwata, H., Conte, P., Mayer, I.A., Kaufman, B., et al. (2019). Alpelisib for *PIK3CA* -mutated, hormone receptor–positive advanced breast cancer. N. Engl. J. Med. *380*, 1929–1940. https://doi.org/10.1056/NEJMoa1813904.
32. Skorda, A., Bay, M.L., Hautaniemi, S., Lahtinen, A., and Kallunki, T. (2022). Kinase inhibitors in the treatment of ovarian cancer: current state and future promises. Cancers *14*, 6257. https://doi.org/10.3390/cancers14246257.
33. Mishra, R., Patel, H., Alanazi, S., Kilroy, M.K., and Garrett, J.T. (2021). PI3K inhibitors in cancer: clinical implications and adverse effects. Int. J. Mol. Sci. *22*, 3464. https://doi.org/10.3390/ijms22073464.
34. Senkowski, W., Gall-Mas, L., Falco, M.M., Li, Y., Lavikka, K., Kriegbaum, M.C., Oikkonen, J., Bulanova, D., Pietras, E.J., Voßgröne, K., et al. (2023). A platform for efficient establishment, expansion and drug response profiling of high-grade serous ovarian cancer organoids. Dev Cell. https://doi.org/10.1016/j.devcel.2023.04.012.
35. Hu, Z., Li, Z., Ma, Z., and Curtis, C. (2020). Multi-cancer analysis of clonality and the timing of systemic spread in paired primary tumors and metastases. Nat. Genet. *52*, 701–708. https://doi.org/10.1038/s41588-020-0628-z.
36. Janiszewska, M., Tabassum, D.P., Castaño, Z., Cristea, S., Yamamoto, K.N., Kingston, N.L., Murphy, K.C., Shu, S., Harper, N.W., del Alcazar, C.G., et al. (2019). Subclonal cooperation drives metastasis by modulating local and systemic immune microenvironments. Nat. Cell Biol. *21*, 879–888. https://doi.org/10.1038/s41556-019-0346-x.
37. Konstantinopoulos, P.A., Gonzalez-Martin, A., Cruz, F.M., Friedlander, M., Glasspool, R., Lorusso, D., Marth, C., Monk, B.J., Kim, J.-W., Hinson, P., et al. (2022). EPIK-O/ENGOT-OV61: alpelisib plus olaparib vs cytotoxic chemotherapy in high-grade serous ovarian cancer (phase III study). Future Oncol. *18*, 3481–3492. https://doi.org/10.2217/fon-2022-0666.
38. Cancer Genome Atlas Research Network (2011). Integrated genomic analyses of ovarian carcinoma. Nature *474*, 609–615. https://doi.org/10.1038/nature10166.
39. Kaipio, K., Chen, P., Roering, P., Huhtinen, K., Mikkonen, P., Östling, P., Lehtinen, L., Mansuri, N., Korpela, T., Potdar, S., et al. (2020). ALDH1A1-related stemness in high-grade serous ovarian cancer is a negative prognostic indicator but potentially targetable by EGFR/mTOR-PI3K/aurora kinase inhibitors. J. Pathol. *250*, 159–169. https://doi.org/10.1002/path.5356.
40. Bolger, A.M., Lohse, M., and Usadel, B. (2014). Trimmomatic: a flexible trimmer for Illumina sequence data. Bioinformatics *30*, 2114–2120. https://doi.org/10.1093/bioinformatics/btu170.
41. Andrews, S. (2015). FastQC.
42. Li, H. (2013). Aligning Sequence Reads, Clone Sequences and Assembly Contigs with BWA-MEM.
43. McKenna, A., Hanna, M., Banks, E., Sivachenko, A., Cibulskis, K., Kernytsky, A., Garimella, K., Altshuler, D., Gabriel, S., Daly, M., and DePristo, M.A. (2010). The Genome Analysis Toolkit: a MapReduce framework for analyzing next-generation DNA sequencing data. Genome Res. *20*, 1297–1303. https://doi.org/10.1101/gr.107524.110.
44. DePristo, M.A., Banks, E., Poplin, R., Garimella, K. v, Maguire, J.R., Hartl, C., Philippakis, A.A., del Angel, G., Rivas, M.A., Hanna, M., et al. (2011). A framework for variation discovery and genotyping using next-generation DNA sequencing data. Nat. Genet. *43*, 491–498. https://doi.org/10.1038/ng.806.
45. Quinlan, A.R. (2014). BEDTools: the Swiss-army tool for genome feature analysis. Curr. Protoc. Bioinformatics *47*, 11.12.1–11.1234. https://doi.org/10.1002/0471250953.bi1112s47.
46. Quinlan, A.R., and Hall, I.M. (2010). BEDTools: a flexible suite of utilities for comparing genomic features. Bioinformatics *26*, 841–842. https://doi.org/10.1093/bioinformatics/btq033.
47. van der Auwera, G., and O'Connor, B.D. (2020). Genomics in the Cloud: Using Docker, GATK, and WDL in Terra, 1st ed.
48. Karczewski, K.J., Francioli, L.C., Tiao, G., Cummings, B.B., Alföldi, J., Wang, Q., Collins, R.L., Laricchia, K.M., Ganna, A., Birnbaum, D.P., et al. (2020). The mutational constraint spectrum quantified from variation in 141,456 humans. Nature *581*, 434–443. https://doi.org/10.1038/s41586-020-2308-7.
49. Zhang, F., Flickinger, M., Taliun, S.A.G., InPSYght Psychiatric Genetics Consortium, Abecasis, G.R., Scott, L.J., McCaroll, S.A., Pato, C.N., Boehnke, M., and Kang, H.M. (2020). Ancestry-agnostic estimation of DNA sample contamination from sequence reads. Genome Res. *30*, 185–194. https://doi.org/10.1101/gr.246934.118.
50. Kitts, A., Phan, L., and Ward, M. (2013). In The Database of Short Genetic Variation (dbSNP, 2nd edition, A. Kitts, L. Phan, and M. Ward, eds. (National Center for Biotechnology Information).
51. Sherry, S.T., Ward, M.H., Kholodov, M., Baker, J., Phan, L., Smigielski, E.M., and Sirotkin, K. (2001). dbSNP: the NCBI database of genetic variation. Nucleic Acids Res. *29*, 308–311. https://doi.org/10.1093/nar/29.1.308.
52. Rentzsch, P., Schubach, M., Shendure, J., and Kircher, M. (2021). CADD-Splice-improving genome-wide variant effect prediction using deep learning-derived splice scores. Genome Med. *13*, 31. https://doi.org/10.1186/s13073-021-00835-9.
53. Wang, K., Li, M., and Hakonarson, H. (2010). ANNOVAR: functional annotation of genetic variants from high-throughput sequencing data. Nucleic Acids Res. *38*, e164. https://doi.org/10.1093/nar/gkq603.
54. Pruitt, K.D., Brown, G.R., Hiatt, S.M., Thibaud-Nissen, F., Astashyn, A., Ermolaeva, O., Farrell, C.M., Hart, J., Landrum, M.J., McGarvey, K.M., et al. (2014). RefSeq: an update on mammalian reference sequences. Nucleic Acids Res. *42*, D756–D763. https://doi.org/10.1093/nar/gkt1114.
55. Navarro Gonzalez, J., Zweig, A.S., Speir, M.L., Schmelter, D., Rosenbloom, K.R., Raney, B.J., Powell, C.C., Nassar, L.R., Maulding, N.D., Lee, C.M., et al. (2021). The UCSC Genome Browser database: 2021 update. Nucleic Acids Res. *49*, D1046–D1057. https://doi.org/10.1093/nar/gkaa1070.
56. Landrum, M.J., Lee, J.M., Benson, M., Brown, G.R., Chao, C., Chitipiralla, S., Gu, B., Hart, J., Hoffman, D., Jang, W., et al. (2018). ClinVar: improving access to variant interpretations and supporting evidence. Nucleic Acids Res. *46*, D1062–D1067. https://doi.org/10.1093/nar/gkx1153.
57. Tate, J.G., Bamford, S., Jubb, H.C., Sondka, Z., Beare, D.M., Bindal, N., Boutselakis, H., Cole, C.G., Creatore, C., Dawson, E., et al. (2019). COSMIC: the catalogue of somatic mutations in cancer. Nucleic Acids Res. *47*, D941–D947. https://doi.org/10.1093/nar/gky1015.
58. Amemiya, H.M., Kundaje, A., and Boyle, A.P. (2019). The ENCODE blacklist: identification of problematic regions of the genome. Sci. Rep. *9*, 9354. https://doi.org/10.1038/s41598-019-45839-z.
59. van Loo, P., Nordgard, S.H., Lingjærde, O.C., Russnes, H.G., Rye, I.H., Sun, W., Weigman, V.J., Marynen, P., Zetterberg, A., Naume, B., et al. (2010). Allele-specific copy number analysis of tumors. Proc. Natl. Acad. Sci. USA *107*, 16910–16915. https://doi.org/10.1073/pnas.1009843107.
60. Mermel, C.H., Schumacher, S.E., Hill, B., Meyerson, M.L., Beroukhim, R., and Getz, G. (2011). GISTIC2.0 facilitates sensitive and confident localization of the targets of focal somatic copy-number alteration in human cancers. Genome Biol. *12*, R41. https://doi.org/10.1186/gb-2011-12-4-r41.
61. O'Leary, N.A., Wright, M.W., Brister, J.R., Ciufo, S., Haddad, D., McVeigh, R., Rajput, B., Robbertse, B., Smith-White, B., Ako-Adjei, D., et al. (2016). Reference sequence (RefSeq) database at NCBI: current status, taxonomic expansion, and functional annotation. Nucleic Acids Res. *44*, D733–D745. https://doi.org/10.1093/nar/gkv1189.

62. Gillis, S., and Roth, A. (2020). PyClone-VI: scalable inference of clonal population structures using whole genome data. BMC Bioinf. *21*, 571. https://doi.org/10.1186/s12859-020-03919-2.

63. Wang, Y., Lawson, C.L., and Hanson, R.J. (2020). Lsei: Solving Least Squares or Quadratic Programming Problems under Equality/Inequality Constraints.

64. Dang, H.X., White, B.S., Foltz, S.M., Miller, C.A., Luo, J., Fields, R.C., and Maher, C.A. (2017). ClonEvol: clonal ordering and visualization in cancer sequencing. Ann. Oncol. *28*, 3076–3082. https://doi.org/10.1093/annonc/mdx517.

65. Gundem, G., van Loo, P., Kremeyer, B., Alexandrov, L.B., Tubio, J.M.C., Papaemmanuil, E., Brewer, D.S., Kallio, H.M.L., Högnäs, G., Annala, M., et al. (2015). The evolutionary history of lethal metastatic prostate cancer. Nature *520*, 353–357. https://doi.org/10.1038/nature14347.

66. Martincorena, I., Raine, K.M., Gerstung, M., Dawson, K.J., Haase, K., van Loo, P., Davies, H., Stratton, M.R., and Campbell, P.J. (2017). Universal patterns of selection in cancer and somatic tissues. Cell *171*, 1029–1041.e21. https://doi.org/10.1016/j.cell.2017.09.042.

67. Yang, Y.R., Vuitton, D.A., Jones, M.K., Craig, P.S., and McManus, D.P. (2005). Can the strengths of AIC and BIC be shared? A conflict between model indentification and regression estimation. Biometrika *99*, 937–941. https://doi.org/10.1093/biomet/92.4.937.

68. Jassal, B., Matthews, L., Viteri, G., Gong, C., Lorente, P., Fabregat, A., Sidiropoulos, K., Cook, J., Gillespie, M., Haw, R., et al. (2020). The reactome pathway knowledgebase. Nucleic Acids Res. *48*, D498–D503. https://doi.org/10.1093/nar/gkz1031.

69. Yu, G., and He, Q.-Y. (2016). ReactomePA: an R/Bioconductor package for reactome pathway analysis and visualization. Mol. Biosyst. *12*, 477–479. https://doi.org/10.1039/C5MB00663E.

70. Liao, J.G., and Rosen, O. (2001). Fast and stable algorithms for computing and sampling from the noncentral hypergeometric distribution. Am. Statistician *55*, 366–369. https://doi.org/10.1198/000313001753272547.

71. Cantor, J.R., Abu-Remaileh, M., Kanarek, N., Freinkman, E., Gao, X., Louissaint, A., Lewis, C.A., and Sabatini, D.M. (2017). Physiologic medium rewires cellular metabolism and reveals uric acid as an endogenous inhibitor of UMP synthase. Cell *169*, 258–272.e17. https://doi.org/10.1016/j.cell.2017.03.023.

STAR★METHODS

KEY RESOURCES TABLE

REAGENT or RESOURCE	SOURCE	IDENTIFIER
Antibodies		
Mouse anti-Ki67 Antigen, clone MM1 (monoclonal)	Monsanto	Cat# MONX10283; RRID: AB_1833494
E-Cadherin (24E10) Rabbit mAb	Cell Signaling Technology	Cat# 3195S; RRID: AB_2291471
E-Cadherin (ab11512), Rat mAb [DECMA-1]	Abcam	Cat# ab11512; RRID: AB_298118
Goat anti-Rat IgG (H+L) Secondary Antibody, Alexa Fluor 488	Invitrogen	Cat# A-11006; RRID: AB_2534074
Donkey anti-Mouse IgG (H+L), Alexa Fluor 594	Thermo Fisher Scientific	Cat# A21203; RRID: AB_141633
Donkey anti-Rabbit IgG (H+L), Alexa Fluor 488	Life Technologies	Cat# A-21206; RRID: AB_2535792
Biological samples		
Fresh-frozen tissue samples	This paper	N/A
Ascites samples	This paper	N/A
H&E-stained FFPE tissue sections	This paper	N/A
Plasma	This paper	N/A
Patient-derived cell cultures	This paper	N/A
Chemicals, peptides, and recombinant proteins		
Advanced DMEM/F-12	Thermo Fisher Scientific	Cat# 12634028
Plasmax™	Ximbio	Cat# 156371
Phosphate buffered saline	Gibco	Cat# 10010023
TrypLE™ Express	Gibco	Cat# 12604013
GlutaMAX	Gibco	Cat# 35050038
HEPES, pH. 7.4	homemade	N/A
2-hydroxybutyric acid	Sigma-Alrdich	Cat# 220116-5G
Primocin	InvivoGen	Cat# ant-pm-1
B-27™ Supplement (50X), minus vitamin A	Thermo Fischer Scientific	Cat# 12587010
p38/SAPK2 Inhibitor (SB202190)	MedChemExpress	Cat# HY-10295
A-83-01	Sigma-Alrdich	Cat# SML0788
β-Estradiol	Merck	Cat# E2758
Recombinant Human FGF-10	Peprotech	Cat# 100-26
Recombinant Human FGF-4	Peprotech	Cat# 100-31
Recombinant Human Heregulinβ-1	Peprotech	Cat# 100-03
Animal-Free Recombinant Human EGF	Peprotech	Cat# AF-100-15
Hydrocortisone	Sigma-Aldrich	Cat# H0888
Forskolin	MedChemExpress	Cat# HY-15371
N-acetyl-cysteine	Sigma-Aldrich	Cat# A9165
Nicotinamide	Merck	Cat# N0636
Y-27632	MedChemExpress	Cat# HY-10583
Propidium iodide solution	Sigma-Aldrich	Cat# P4864
Hoechst-33342, bisBenzimide H, 33342 Trihydrochloride	Sigma-Aldrich	Cat# B2261
Hoechst-33258, bisBenzimide H 33258 Trihydrochloride	Sigma-Aldrich	Cat# 861405
DMSO (Dimethyl Sulfoxide)	Avantor	Cat# AMREN182
Alpelisib (BYL719)	Selleck Chemicals	Cat# S2814
Alpelisib	MedChemExpress	Cat# HY-15244
Idelalisib	Selleck Chemicals	Cat# S2226
Idelalisib	MedChemExpress	Cat# HY-13026
Umbralisib	MedChemExpress	Cat# HY-12279

(*Continued on next page*)

Continued

REAGENT or RESOURCE	SOURCE	IDENTIFIER
Bortezomib	Selleck Chemicals	Cat# PS-341
Glycine	Sigma-Aldrich	Cat# G7126
Bovine Serum Albumin (BSA)	Sigma-Aldrich	Cat# AG3059
Triton100X	Sigma-Aldrich	Cat# T9284)
Tween 20	Sigma-Aldrich	Cat# 274348
Cultrex Reduced Growth Factor Basement Membrane Extract, Type 2	R&D Systems and Amsbio	Cat# 3533-010-02
Critical commercial assays		
Chemagic DNA Blood Kit Special	PerkinElmer Inc.	CMG-1091
DNBSEQ (BGISEQ-500/MGISEQ-2000)	MGI Tech Co. Ltd.	https://en.mgi-tech.com/products/
HiSeq X Ten	Illumina	https://www.illumina.com/systems/sequencing-platforms/hiseq-x.html
RiboZero Kit	Illumina	20037135
Deposited data		
Raw DNA sequence data	This paper	EGAS00001006775
Raw bulk RNA-seq sequence data	This paper	EGAS00001004714
Patient clinical data	This paper	https://doi.org/10.5281/Zenodo.7852210
TCGA genomic data	Genomic Data Commons	https://portal.gdc.cancer.gov/
Experimental models: Cell lines		
Patient-derived organoids	Laboratory of Krister Wennerberg	N/A
Software and algorithms		
Anduril 2.0-7e2341d	(Cervera et al., 2019)[14]	https://anduril.org
Adobe Illustrator	Adobe	www.adobe.com
Affinity Designer	Serif	https://affinity.serif.com/en-us/
BioRender	BioRender	https://biorender.com/
Trimmomatic 0.32	(Bolger et al., 2014)[40]	http://www.usadellab.org/
FastQC v0.11.4	(Andrews, 2015)[41]	https://www.bioinformatics.babraham.ac.uk/projects/fastqc/
BWA-MEM 0.7.12-41039	(Li, 2013)[42]	http://bio-bwa.sourceforge.net/
SAMtools	(Danecek et al., 2021; Li et al., 2009)	http://www.htslib.org/
Picard 2.6	Broad Institute	https://github.com/broadinstitute/picard
GATK	(McKenna et al., 2010)[43]	https://gatk.broadinstitute.org/hc/en-us
ASCAT v2.5.2	(van Loo et al., 2010)[59]	https://github.com/VanLoo-lab/ascat/releases
BEDtools 2.28.0	(Quinlan, 2014; Quinlan & Hall, 2010)[45,46]	https://bedtools.readthedocs.io/en/latest/
GISTIC 2.0.23	(Mermel et al., 2011)[60]	https://bioinformaticshome.com/tools/cnv/descriptions/GISTIC.html
PyClone-VI	(Gillis & Roth, 2020)[62]	https://github.com/Roth-Lab/pyclone-vi
PRISM v0.9	(Häkkinen et al., 2021)[25]	https://bitbucket.org/anthakki/prism/
CADD v1.6	(Rentzsch et al., 2021)[52]	https://cadd.gs.washington.edu/download
ANNOVAR 20191024	(K. Wang et al., 2010)[53]	https://annovar.openbioinformatics.org/
SePIA	(Icay et al., 2016)	https://anduril.org/sepia/
STAR v2.5.2b	(Dobin et al., 2013)	https://github.com/alexdobin/STAR
eXpress v 1.5.1-linux_x86_64	(Roberts & Pachter, 2013)	https://pachterlab.github.io/eXpress/
MATLAB and Statistics Toolbox Release 2012b	The MathWorks, Inc.	http://www.matlab.com/
R versions 3.6.3 and higher	R Core Team	https://www.r-project.org
R package dNdScv v 0.0.1.0	(Martincorena et al., 2017)[66]	https://github.com/im3sanger/dndscv
R package ClonEvol v0.99.11	(Dang et al., 2017)[64]	https://github.com/hdng/clonevol

(*Continued on next page*)

Continued

REAGENT or RESOURCE	SOURCE	IDENTIFIER
R package ReactomePA v1.38.0	(Yu & He, 2016)[69]	https://bioconductor.org/packages/release/bioc/html/ReactomePA.html
R package fgsea v1.12.0	Bioconductor	https://doi.org/10.1101/060012, http://biorxiv.org/content/early/2016/06/20/060012
R package lsei v 1.3-0	(Y. Wang et al., 2020)[63]	https://cran.r-project.org/web/packages/lsei/index.html
R package Seurat v2.3.4	(Butler et al., 2018)	https://satijalab.org/seurat/
R package survival v3.1-12	CRAN	https://github.com/therneau/survival
R package tidyverse v1.3.1	CRAN	https://tidyverse.tidyverse.org/
R package R.utils v2.12.0	CRAN	https://henrikbengtsson.github.io/R.utils/
Fiji (ImageJ)	(Schneider et al. 2012)	https://imagej.nih.gov/ij/index.html
GraphPad Prism 9.0.0	GraphPad	https://www.graphpad.com/scientific-software/prism/
MetaXpress 387 High-Content Image Acquisition and Analysis Software	Molecular Devices	https://www.moleculardevices.com/products/cellular-imaging-systems/acquisition-and-analysis-software/metaxpress
ImageXpress Confocal HT.ai	Molecular Devices	https://www.moleculardevices.com/products/cellular-imaging-systems#High-Content-Imaging
GenomeSpy	This paper	https://genomespy.app/doi: 10.5281/zenodo.7852282
Nested pathway, clustering, and heterogeneity related algorithms, GenomeSpy specifications and data, and other custom scripts related to this paper.	This paper	https://doi.org/10.5281/zenodo.7852210
Other		
384 Well, Black/Clear, Tissue Culture Treated, FalconFlat Bottom with lid Imaging plates	Falcon	Cat# 353962
Screenstar, 96 Well Microplate, Black, 190 μm Clear Bottom, Cell Culture Treated Imaging plates	Greiner	Cat# 655866

RESOURCE AVAILABILITY

Lead contact

Further information and requests for resources and reagents should be directed to and will be fulfilled by the lead contact, Jaana Oikkonen (jaana.oikkonen@helsinki.fi).

Materials availability

This study did not generate new unique reagents.

Data and code availability

- All raw DNA sequencing data is submitted to the European Genome-phenome Archive (EGA) and will be publicly available under study accession number EGAS00001006775. Raw bulk RNA sequencing data are deposited in the EGA and are publicly available (EGAS00001004714).
- Code is publicly available from Github repository https://github.com/HautaniemiLab/tumor-evolution-2023 (https://doi.org/10.5281/zenodo.7852210).
- Any additional information required to reanalyze the data reported in this paper is available from the lead contact upon request.

EXPERIMENTAL MODEL AND SUBJECT DETAILS

Cohort description

HGSC cohort comprised 148 female patients (*N*, discovery = 55; *N*, validation = 93), selected from the DECIDER cohort (NCT04846933), and treated at Turku University Hospital, Finland, from March 2014 to May 2019. The treatment was either primary debulking surgery (PDS), followed by a median of six cycles of platinum-taxane chemotherapy, or neoadjuvant chemotherapy (NACT), where primary laparoscopic operation with diagnostic tumor sampling was followed by a median of three cycles of NACT

including carboplatin and paclitaxel. In NACT-treated patients, interval debulking surgery aiming at complete cytoreduction was performed after NACT. All patients participating in the study gave their informed consent, and the study was approved by the Ethics Committee of the Hospital District of Southwest Finland (ETMK 145/1801/2015).

Sample selection

For this study we used 510 samples from fresh-frozen solid tumor tissues and ascites, details listed in Table S1. Tumor samples originated from tubo-ovarian tissue (ovaries and fallopian tubes), intra-abdominal tissue (omentum, peritoneum, bowel, and mesenterium), other sites (most commonly lymph nodes, liver, vagina, and pleural fluid), and ascites. The treatment phases represented diagnostic samples collected prior to treatment, interval samples obtained after NACT, and relapse samples collected at progression. All patients had at least two samples with estimated purity > 5% from either different treatment phases or different sites. As some downstream analyses expect each patient to be represented by exactly one sample, we chose one fresh-frozen sample for each patient using the following prioritization: 1) Treatment-naïve metastasis, 2) Treated metastasis, 3) Treatment-naïve tubo-ovarian, 4) Treated tubo-ovarian, 5) Ascites or pleural fluid. If multiple choices were available, e.g., a patient had two treatment-naïve metastasis samples, the one with the highest purity was chosen. The representative samples are indicated by a metadata attribute in the GenomeSpy visualization.

Patient-derived cell lines

Seven primary patient-derived cell cultures were established in spheroidal DMEM-F12 medium (Thermo Fisher Scientific, USA), as described in,[39] and were sampled for sequencing. The cultured cells were characterized by next-generation sequencing and verified to be tumorous based on a known *TP53*-mutation.

Patient-derived organoid culture

Five established patient-derived HGSC tumor organoids EOC733_pPer1, EOC733_iOme, EOC989_r1Asc, EOC989_iOme, and EOC1120_pOme1 were provided by Wojciech Senkowski from the professor Krister Wenneberg's laboratory (Biotech Research & Innovation Center (BRIC), Copenhagen University) as frozen stock suspensions. Organoids were thawed at room temperature (RT), mixed with 2 ml of advanced DMEM/F12 (Gibco) basal growth medium and centrifuged at 240 RCF for 5 min. Freezing medium (Stem Cell Banker; Amsbio, #11894) was discarded and organoids consisted of approximately 10^6 cells/ml were resuspended in 200 μl of cold 7.5 ng/ml Cultrex Reduced Growth Factor Basement Membrane Extract, type 2, Pathclear (BME-2; Amsbio/R&D Systems, #3533-010-02), after the exact BME-2 concentration was adjusted with cold PBS (Gibco, #10010023). Organoids were seeded as 20 μl liquid droplets in pre-warmed 6-well Nunclon™ Delta Surface tissue culture plates (Thermo Scientific, #140675) and 10 droplets were formed per well. The droplets were then solidified after incubation at 37°C for 45 min (forming so called BME-2-embeded organoid spheres) and finally 3 ml of the indicated growth medium supplemented with 5 μM of ROCK-I and -II inhibitor Y-27632 (MedChemExpress, #HY-10583) was added. Two different media were used for the growth and expansion of organoid cultures, depending on which medium they were originally established in.[34] EOC1120 organoids were grown in DMEM/F12 medium supplemented with 100 μg/ml Primocin (InvivoGen , #ant-562 pm-1), 10 mM HEPES pH 7.4 (homemade), 1:100-diluted 100x GlutaMAX (Gibco, #35050061), 1:50-diluted 50x B-27 Supplement, minus vitamin A (Thermo Fischer Scientific, #12587010), 0.5 μM SB202190 (MedChemExpress, #HY-10295), 0.5 μM A83-01 (Sigma-Aldrich, #SML0788), 10 ng/ml Recombinant Human FGF-10 (Peprotech, #100-26), 10 ng/ml Recombinant Human FGF-4 (Peprotech, #100-31), 100 nM β-Estradiol (Sigma-Aldrich, #E2758), 5 mM Nicotinamide (Sigma-Aldrich, #N0636) and 1 mM N-acetyl-cysteine (Sigma-Aldrich, #A7250). EOC733 and EOC989 were cultured in the same medium supplemented with 37 ng/ml recombinant human Heregulin β-1 (Peprotech, #100-03), 5 ng/ml animal-free Recombinant Human EGF (Peprotech, #AF-100-15), 500 ng/ml Hydrocortisone (Sigma-Aldrich, #H0888) and 5 μM Forskolin (MedChemExpress, #HY-15371). Organoid cultures were kept in humidified atmosphere of 5% CO_2 at 37°C in a Heraeus Hera Cell CO_2 incubator (AXEB Laboratory Products). Medium was exchanged every 3-4 days.

METHOD DETAILS

Sample preparation

Tumor tissue samples were obtained from laparoscopy and debulking surgery during normal clinical treatment course and were histologically examined by a pathologist. Samples from ovaries and omentum were preferred for diagnostic and interval phases. We used ascites samples when available, especially for the relapses. For germline variation detection we collected blood samples at the beginning of treatment, and DNA was extracted in Auria biobank using Chemagic DNA Blood Kit Special (PerkinElmer Inc., USA) and Chemagic 360 instrument (PerkinElmer Inc., USA). For other samples, Qiagen AllPrep kit was used to extract DNA and RNA simultaneously.

Whole-genome and RNA sequencing

Tissue samples with sufficient DNA/RNA content and quality were sent to library preparation and sequencing to BGI (BGI Europe A/S, Denmark), where whole-genome sequencing (WGS) was performed with either DNBSEQ (BGISEQ-500 or MGISEQ-2000, MGI Tech Co., Ltd., China) or HiSeq X Ten (Illumina, USA) as 150bp paired end sequencing. Median coverage was ~36x (range 24-96x) in the

discovery set and ~51x (range 24-117x) in the validation set. RNA sequencing was performed with DNBSEQ, HiSeq X Ten or Illumina Hiseq 4000 (Illumina, USA) as 100bp or 150bp paired end sequencing.

WGS data preprocessing

We performed WGS analyses using Anduril, a bioinformatics workflow platform developed for large data sets.[14] We trimmed read data using Trimmomatic 0.32[40] and assessed quality with FastQC v0.11.4[41] via Anduril QCFasta v5.0 component. The trimmed reads we aligned using BWA-MEM 0.7.12-41039[42] with option -M against the human reference genome GRCh38.d1.vd1, which was followed by read deduplication using Picard 2.6 (https://github.com/broadinstitute/picard) *DuplicateMarker* and base quality score recalibration using Genome Analysis Toolkit (GATK)[43] version 3.7 *BaseRecalibrator*.[44]

In one batch we filtered vector contamination by aligning first the trimmed reads against the vector sequence, keeping only unmapped reads which were converted back to FASTQ using BEDtools 2.28.0[45,46] *bamtofastq* before proceeding with the alignment as above. We used the following vector sequence for read filtering:

AACAATTTCACACAGGAAACAGCTATGACCATGATTACGCCAAGCTCGAAATTAACCCTCACTAAAGGGAACAAAAGCTGGAGC
TCCACCGCGGTGGCGGCCGCTCTAGAACTAGTGGATCCCCCGGGCTGCAGGAATTCGAT.

Finally, we computed alignment stats using Anduril BamStats component which includes coverage estimation via BEDtools *genomecov*. We also estimated cross-sample contamination using GATK 4.1.4.1 according to the best practices.[47] For the validation cohort, we used GATK 4.1.9.0 with gnomAD v3.0[48] common Finnish SNPs. The primary normal samples of each patient used in variant calling served as the matched normals in the contamination estimation. The contamination of validation cohort normals were further evaluated using VerifyBamID2.[49] We filtered samples with contamination greater than 10% and used a more stringent threshold of 3% for tumor samples in the validation cohort.

Mutation calling in WGS data

Panel of normals

We used a somatic panel of normals (PoN) generated from our blood derived normal samples in somatic variant calling according to GATK best practices. More specifically, we used primary normal samples of each patient with contamination less than 5%. Furthermore, as germline resource we used gnomAD v3.0, including passing variants as well as those only failing the filter 'InbreedingCoeff'. We used GATK 4.1.4.1 and Finnish allele fractions in the discovery cohort and GATK 4.1.9.0 and global allele fractions in the validation cohort.

The discovery PoN comprised 80 DECIDER normals while the validation PoN included 181 DECIDER normals and 99 TCGA normals. We chose the TCGA samples from the NCI Genomic Data Commons (GDC), including the legacy repository, by selecting "TCGA" program name, "blood derived normal" sample type, and "WGS" experimental summary as common criteria. In GDC repository we further specified "illumina" platform, while in the legacy GDC, we selected those with "HiSeq X Ten" platform, "BAM" data format, and "unaligned" or "aligned" data type. We chose the samples on December 22, 2020, totaling the 99 normal samples from TCGA sub-studies: four SARC (sarcoma), 13 ESCA (esophageal carcinoma), and 82 LUAD (lung adenocarcinoma). The data were harmonized to our preprocessing. However, base quality recalibration was not repeated for LUAD data.

Somatic variants

We called somatic short variants by jointly calling multiple tumor samples against a single matched normal for each patient using GATK 4.1.4.1 (4.1.9.0 in validation cohort) *Mutect2* based on best practices. As in PoN, we utilized Finnish gnomAD allele frequencies as germline resource. Variant calling was restricted to primary chromosome assemblies excluding Y chromosome. We filtered the variants using GATK *FilterMutectCalls*, keeping only variants passing all filters. Since somatic calling preceded purity estimation, our per-patient joint calling sample set contained low purity samples excluded from this study. We kept variants that had ALT reads in the retained samples.

In variant annotation we used GATK *VariantAnnotator* to add dbSNP 153(155 in validation cohort)[50,51] IDs and utilized the offline version of Combined Annotation Dependent Depletion (CADD) v1.6[52] with an in-house solution to write into variant call format files. We computed variant allele frequencies (VAF) from reference and alternate (ALT) allele read depth (AD) field. Finally, we used ANNOVAR 20191024[53] to include the following annotations: refGene[54] dated 2020-03-01 (2020-08-17 in validation cohort), downloaded from the University of California, Santa Cruz (UCSC) genome browser database[55] and available online at https://hgdownload.soe.ucsc.edu/goldenPath/hg38/database/, as well as other annotations converted for ANNOVAR including ClinVar 20200506 (20220816 in validation cohort),[56] customized annotations for COSMIC v91 (v96 in validation cohort),[57] and gnomAD v3.0 genomes.

Germline variants

We called germline short variants using GATK 4.1.4.1 (4.1.9.0 in validation cohort) joint genotyping approach following best practices. More specifically, we used GATK *HaplotypeCaller* to call in genomic variant call format (GVCF) on individual normal samples from a set of DECIDER normal samples (*N*, discovery = 80; *N*, validation = 217) with allele-specific annotations before merging and genotyping with *GenotypeGVCFs*. We restricted variant calling to primary nuclear chromosome assemblies excluding Y chromosome. In variant allele filtering, we used allele-specific variant quality score recalibration, dropping all filtered ALT alleles from subsequent analyses.

We further refined the genotype calls using GATK *CalculateGenotypePosteriors* and filtered genotypes with genotype quality (GQ) less than 20 and read depth (DP) less than 10. We then filtered dubious genotype calls by requiring the sum of depths for genotyped allele reads be a minimum of 5 and VAF of genotyped alleles be at least 20% (AlleleBalance filter), both computed from the AD field.

Calling copy-number variants from WGS data

We used the GATK[43] version 4.1.4.1 to perform the copy-number segmentation. To collect the minor allele counts (BAF), we used all filtered biallelic germline SNPs with heterozygous calls (VAF between 40% and 60%) from each patient. Read-count collection used one kilobase intervals. Both read and allelic count collection excluded regions listed in the ENCODE blacklist.[58] To denoise the read counts, we used platform specific (HiSeq, DNBSEQ, and NovaSeq) panels of normals built from the normal samples. After the segmentation, we used ASCAT v2.5.2[59] to estimate purity, ploidy, and allele-specific copy numbers. Since ASCAT does not readily accept pre-segmented data, we converted the segmented data into "faked" SNPs readable by ASCAT. We also used VAFs of the *TP53* mutations as additional evidence for the optimal ploidy/purity selection. Since all the patients had homozygous *TP53* mutations in their cancer cells, we could use the *TP53* VAF and its total copy number (CN) to calculate a *TP53*-based purity:

$$\text{purity}_{TP53} = 2 / ((CN / VAF) - (CN - 2))$$

When ASCAT and *TP53*-based purities disagreed, we chose the higher one. Samples without aberrant CNV model were excluded from further analyses.

The validation cohort comprises more recent data and was analyzed using a slightly improved pipeline. In addition to the ENCODE blacklist, we applied our internal DECIDER blacklist comprising poorly aligned regions and population-level copy-number variance. It is based on regions having abs(logR) > 0.2 in at least three of the 114 normal samples used in its generation. The blacklist is available in the GenomeSpy visualization as an annotation track. Moreover, instead of generating "faked" SNPs for ASCAT, we reimplemented the ASCAT algorithm so that it readily inputs segmented data and directly penalizes solution candidates that disagree with the *TP53*-based purity. Otherwise, the discovery and validation pipelines were identical.

As the contribution of non-aberrant cells on the logR and BAF values encumber downstream analyses, we calculated "purified" values, *i.e.,* removed the non-aberrant component, using the following formulas.

Purified R, based on discussion in https://github.com/lima1/PureCN/issues/40:

$$\text{purifiedR} = (\text{purity} \times \text{ploidy} \times R + 2 \times (1 - \text{purity}) \times (R - 1))/(\text{purity} \times \text{ploidy})$$

Purified BAF, derived from S2, S7, and S8 of (van Loo et al., 2010):

$$f(af) = \text{purity} - 1 + R \times af \times (2 \times (1 - \text{purity}) + \text{purity} \times \text{ploidy})$$

$$\text{purifiedBaf} = f(baf)/(f(1 - baf) + f(baf))$$

GISTIC analysis

We ran GISTIC 2.0.23[60] with the default parameters for all 55 patients belonging to the discovery cohort using the representative samples and purified logR values. We applied the above-mentioned DECIDER blacklist in the GISTIC analysis phase as it was not used in the copy-number segmentation of the discovery cohort.

GenomeSpy visualization

All genomics and key clinical data accompanied by bookmarks are available via an interactive visualization tool GenomeSpy (https://genomespy.app/) at https://csbi.ltdk.helsinki.fi/p/lahtinen_et_al_2023/. In brief, we specified a visualization that comprises copy-number variation (purified logR values), loss of heterozygosity (defined as abs(purified BAF – 0.5) × 2), somatic short variants (SSVs), essential metadata such as clinical variables, and GISTIC results. Only those SSVs were included that had a CADD score greater or equal to 10.0 or were pathogenic according to ClinVar. The visualization contains additional tracks that provide context for the genomic data: cytobands, ENCODE Blacklist,[58] RefSeq Gene annotations,[61] and COSMIC Cancer Gene Census.[15]

Subclonal mutations

For subclonal clustering, we included only mutations that had 1) CNV segment information in all samples, 2) at least two ALT reads in a tumor sample, 3) no ALT reads in matched normal sample, 4) median coverage at least 20, and 5) minimum 15 reads in every sample of that patient. Mutations were divided into cancer cell fraction (CCF) clusters using PyClone-VI.[62] It corrects for copy-number status of the mutations and estimates CCF status across samples. We estimated the model for a maximum of 30 clusters and used 100 restarts. The primary run was performed using only single base substitutions (SBS). Indels (short insertions and deletions) were fitted to the clusters via a secondary run with reduced weight for the indels: indel read counts were divided by 2. Indels from secondary clusters were merged into original clusters when the clusters had at least 70% overlap in SBS. Original, SBS based cellular frequencies were used in downstream analyses. Indels have less reliable VAF values, and this protocol was used to build the most reliable clusters.

Subclonal cluster filtering

We kept clusters with 5% minimum CCF in at least one sample. The founding cluster was estimated from the cellular frequencies as the most frequent one across samples. Additional clusters with higher CCF than that of the founding cluster (allowing for 5 percentage point error) were excluded. Mutations with cluster assignment probability less than 0.6 or, if smaller, the median probability within the sample were excluded.

For further filtering of clusters with an excess of likely artifact mutations, we employed mutational signature analysis combined with additional variant filtering. For mutational signature analysis, we generated cluster mutational spectra from their non-mitochondrial single nucleotide variants (SNVs) as well as patient spectra from their sums. We fitted signatures using the function pnnls from R package lsei[63] against COSMIC v3.1 signatures corrected for GRCh38 trinucleotide frequency excluding chromosomes Y and M. Signature selection was based on SigProfilerAttribution[17] with backward and forward selection evaluating cosine similarity with thresholds 0.01 and 0.05 respectively as well as connected signature and forced signatures (SBS1 and SBS5) rules. Briefly, we started with common ovarian cancer signatures SBS1, SBS2, SBS3, SBS5, SBS12, and SBS40 and fit the patient level spectra. The patient signatures together with common signatures were initial signatures for preliminary cluster signature selection, the result of which were used as inputs for the final patient level signature selection but with a less stringent backward selection threshold of 0.001. The resultant patient signatures were used as inputs for the final individual cluster signature selection of the respective patient.

As additional filters, we removed variants with NALOD less than 1.0 or CONTQ less than 10 as well as those present in an extended PoN generated with maximum germline probability set to 1.0. The extended PoN for the discovery cohort was generated from 105 DECIDER and the 99 TCGA normals using GATK 4.1.9.0 and global allele frequencies from gnomAD v3.0.

To filter clusters, we utilized the additional filters with signature fitting in three analysis combinations: runs with 1) extra forced signatures with extended filtering, 2) extra forced signatures, and 3) neither. The extra forced signatures were SBS34, SBS41, SBS47, SBS57, SBS58, and SBS90, which were common among spurious clusters. We computed the proportion of artifact mutations in clusters as the total fractional contribution of signatures SBS34, SBS41, SBS47, SBS57, SBS58, SBS90, and SBS7c. We then computed the cluster artefact score (a) as a weighted average, using cosine similarity of fit, of artefact proportion of runs 2 and 3. We also computed the proportion of likely artefacts (b) by summing the fraction of variants excluded by the additional filters and the proportional contribution of artefact signatures of run 1 scaled by the fraction of passing variants. Clusters with an artefact score (a) greater than or equal to 0.25 and proportion of likely artefacts (b) greater than or equal to 0.50 were filtered, as were clusters with fewer than 30 SNVs after variant filters of run 1.

After all filters, 427 clusters remained (77.5% of all clusters) in the discovery cohort and 710 (78.1%) in the validation cohort.

Phylogenetic trees

Mutational trees for all patients were estimated from clustered mutations with ClonEvol.[64] Frequency threshold of 1% was used as a positive threshold for a cluster to exist in a sample. A solution that included the maximum number of clusters was selected. Clusters that were not fitted to tree in the primary run, were refitted allowing 5 percentage point error in their estimated frequency until no further clusters could be fitted. When multiple options with the maximum number of clusters were available, solutions excluding smallest (least mutations) or truncal-like clusters, were favored. The truncal-like clusters were assumed to be possible errors in clustering, and they were identified by having in all samples CCF of more than half of that of the founding cluster. When multiple trees were available for same clusters, the best tree was selected using pigeon-hole principle.[65] 76% of the 427 discovery cohort clusters and 76% of the 710 validation cohort clusters were fitted to the trees.

Mouse contamination filter

We observed mouse contamination in three tumor samples (EOC423_pOme2, EOC1120_pPer1, and EOC1129_pPer2) affecting somatic calling results, which resulted in two of these samples having a spurious cluster each. The two clusters were removed as a result. To minimize the effect of contamination in other downstream analyses, we realigned the corresponding BAMs against a concatenated reference genome of GRCh38.d1.vd1 and mouse genome build GRCm39 (toplevel) where the mouse contigs served as decoys. We also reran duplication marking. With the realigned BAMs, we force-called mutations private to the contaminated samples using *Mutect2* in the affected patients, otherwise with the same parameters as in the original somatic variant calling. We tagged variants that no longer had ALT reads in the realigned samples and removed them in downstream analyses.

Jellyfish plots

Phylogeny and clonal compositions estimated by ClonEvol served as input for the patients' jellyfishes (discovery cohort only). We extracted the clonal compositions from the ClonEvol data structures and used a depth-first search on the phylogenetic tree to find a consistent order for the subclones. A consistent order is essential, as it prevents the tentacles (the lines connecting the samples and subclones) from getting entangled. Subsequently, the clonal compositions of each patient were plotted as stacked bar charts using the R package ggplot2 and exported as Scalable Vector Graphics format for manual editing and annotation in Affinity Designer (RRID:SCR_016952). Manual editing involved placing the samples on the canvas according to the different sampling time points, drawing the bells (that illustrate logistic growth) with the nested structure illustrating the inferred phylogeny, adding the tentacles connecting the samples, and adding the putative driver genes.

Frequently mutated genes

We analyzed frequently somatically mutated genes using dNdScv[66] to correct the background mutation rate of each gene. Since the tool requires mutations to be independent, we used patient representative samples (N, discovery = 55; N, validation = 93). Furthermore, phased pairs of variants from *Mutect2* with less than 10 bases between the last affected base of the first variant and the position of the next variant were merged as complex substitutions. We ran dNdScv with Y chromosome genes excluded and using GRCh38 covariates and RefCDS inputs downloaded from https://github.com/im3sanger/dndscv_data/tree/master/data

on January 27, 2022. Following dNdScv's results, we report patients with missense, nonsense, splice site or complex mutations (incl. indels and multiple nucleotide variants), omitting stop loss SNVs.

Subclonal heterogeneity

We used clonal information obtained via mutation trees of 462 tumor tissue samples from all patients to estimate clonal complexity and divergence.

Clonal complexity

To measure clonal complexity of each individual sample, we quantified the perplexity of the subclonal cancer cell frequency distribution of the corresponding mutation tree. The perplexity is an estimate for the effective number of clones, by taking their cellular frequencies into account and is immune to the number of called clones (e.g., $C = k'$ for k' equifrequent clones regardless of k). The clonal complexity of the j^{th} sample is computed as follows:

$$C_j = exp\left(- \sum_{i=1}^{k} p_{ij} \, log \, p_{ij} \right)$$

where p_{ij} is the normalized frequency of the i^{th} clone over the k clones of the j^{th} sample, and by definition $0 \cdot log(0) = 0$. The clonal complexities were averaged in entropic (logarithmic) space to capture patient, tissue, and phase (diagnostic-interval) specific clonal complexity. We also evaluated patient-tissue specificity within patients and tissues using the logarithmic complexity values. This analysis reveals which tissue sites exhibit heterogeneity within the sample, not across the patient disease.

Clonal divergence

We also measured whether each sample's clonal frequency distribution differs from the others. This was quantified using the Kullback-Leibler divergence of the sample's clonal distribution from the average distribution over all samples of each individual patient. The corresponding perplexity represents the effective number of unique clone changes to a particular sample compared with an average sample of the patient. The clonal divergence of the individual j^{th} sample is computed as follows:

$$D_j = exp\left(- \sum_{i=1}^{k} p_{ij} \, log \, \overline{p}_i - \underbrace{\left(- \sum_{i=1}^{k} p_{ij} \, log \, p_{ij} \right)}_{log \, C_j} \right) \text{ with } \overline{p}_i = \frac{1}{n} \sum p_{ij}$$

where p_{ij} is the normalized frequency of the i^{th} clone over the k clones of the j^{th} sample, $\overline{p}_i$ is the average frequency of i^{th} clone in the reference (the n samples of the patient), and $0 \cdot log(0) = 0$. The clonal divergencies were averaged in entropic (logarithmic) space to determine the global average effect for different tissues sites and their significance.

Statistical analysis of clonal complexity and divergence

We applied variance analysis (ANOVA) to assess if the patients, tissues, and phase components feature distinct, specific degree of heterogeneity in their tumors for both the clonal complexity and divergence. First, we assessed if the patient specific complexity is significant versus the unexplained complexity (the replicate variation excluding patient, tissue, and phase specific variation in these data). We performed a similar test for tissue specific and treatment phase specific complexity versus unexplained complexity. We also tested whether the tissue sites exhibit heterogeneity within the patient specific complexity and vice versa, quantifying changes in specific but distinct tissue sites or patient groups. Similarly, we performed ANOVA of the cross-entropy heterogeneity to determine which factors affect the corresponding clonal divergence. The ANOVA coefficients correspond to logarithmic effective clonal number ratios, i.e., a negative coefficient indicates a decrease and positive increase in the effective number of intratumor or tumor-unique clones.

Clustering patients by heterogeneity measures

A patient stratification was obtained by clustering the patients in the clonal complexity versus clonal divergence space. The clonal complexity $\overline{C}$ and divergence $\overline{D}$ of a patient is the geometric mean of the sample complexities C_j and divergencies D_j of the patient (arithmetic entropic mean), respectively. In particular, when averaged over all the samples, the clonal divergence $\overline{D}$ represents the effective number of unique clone sets within the set of samples of a patient.

Since the clonal divergence $\overline{D}$ can only be unity when a single sample is available from the patient, a weighted K-means clustering approach with object-by-feature specific weights was used (Cordeiro de Amorim & Mirkin, 2012). Specifically, the following distance metric d is implied:

$$d(x_i, \mu_k) = \sum_j w_{ij} (x_{ij} - \mu_{ik})^2$$

giving optimal cluster centroids of:

$$\widehat{\mu}_{ik} = \frac{\sum_{i \text{ s.t. } L_i = k} w_{ij} x_{ij}}{\sum_{i \text{ s.t. } L_i = k} w_{ij}}$$

of weighted averages of the data, where x_{ij} is the j:th component of the i:th sample, w_{ij} is the corresponding weight, μ_k is the centroid of the k:th cluster, and L_i is the label of the i:th sample. The weights are set to zero for missing data and are unity otherwise, implying the missing data have no influence on the clustering along the missing dimension, but can affect the clustering along the others. For visualization purposes, the missing values were imputed with the most likely values (i.e., minimal distance), that is, the corresponding cluster centroid. Note that the imputation occurs post-hoc and does not affect the clustering.

The clonal complexity and divergence were computed for the diagnostic, interval, and relapse samples separately, and the data from the diagnostic samples was used for patient stratification. For the clustering, 1,000 iterations and 1,000 restarts were used. Among the 2D discriminators, $K = 3$ clusters was favored by a series of likelihood ratio tests, which was also the preferred model according to the Akaike Information Criterion.[67]

To assess clonal complexity and divergence in a validation cohort, 296 diagnostic, interval, and relapse samples were analyzed using a similar methodology as the discovery cohort. Clustering of patients in the validation cohort was accomplished by utilizing the weighted K-means clustering model established in the discovery cohort and mapping the 255 diagnostic samples to the pre-existing clusters in the clonal complexity and clonal divergence space.

Estimation of clonal pseudo-age

To quantify the clonal topology, we computed the branch and mutation depth and diameter. The branch depth and diameter are computed from the graph induced by the clonal subdivision tree with unit edge lengths, while for the mutational depth edge lengths with a difference in mutations is used.

The depth is defined as the clonal frequency weighted average distance from the root to the observed clones, while the diameter is the weighted average distance within the observed clones. Specifically, given D_{ij} is the shortest undirected path length from the i:th to the j:th clone and p_i is the observed clonal frequency, the depth is given by:

$$d_1 = e_1^T D p$$

where $e_1 = (1, 0, \ldots)$ is frequency distribution of the root ($i = 1$) and the diameter by:

$$d_2 = p^T D p$$

The branch depth acts as the average pseudo-age in number of clonal subdivisions, the diameter measuring its variance, while the mutational depth and diameter are the corresponding measures of a pseudo-age in the number of mutations. The branch and mutational depth and diameter agreed qualitatively, but we found that the branch depth more accurately captured the clonal tree topology between the samples.

Pathway analyses at the subclonal level

Pathways enriched in the evolutionary states

To explore the biological pathways enriched at the subclonal level in the evolutionary states, we combined branch mutations for all patients included in each of the evolutionary cluster and annotated the corresponding genes (2,349, 2,363, and 2,699 genes for 'evolving', 'maintaining', or 'adaptive' clusters, respectively). The mutations were filtered using CADD score 10, excluding intergenic and benign mutations from ClinVar functional annotation,[56] with only branching mutations ('non-truncal' clusters in the downstream analysis) selected for further analyses. Pathway analysis was performed using Reactome Knowledgebase[68] for selected gene sets and statistical significance of results was defined using a threshold of p value <0.05 (after Benjamini-Hochberg adjustment). Shared pathways were defined as pathways statistically significantly enriched in any two or in all three states. Six unique signaling cascades were defined as cancer pathways a) statistically significant in one of the states and b) including known anticancer drug targets. Analyses were conducted in R software v3.6.3 (https://www.r-project.org/), using R package ReactomePA v1.38.0.[69]

Stability of selected signaling cascades across treatment

The stability of six unique signaling cascades across the treatment was assessed in the samples collected at diagnosis, interval, and relapse phases (149, 43, and 22 samples, respectively). The filtering of mutations and pathway analyses were conducted in the same way, as described above, and statistical significance of results was defined using a threshold of p value <0.05 (after Benjamini-Hochberg adjustment).

Nested pathway analyses

A typical binary enrichment analysis, e.g., of abundance of pathway specific hits, uses the overlap count of the called genes and the genes involved in the pathway and a Fisher's exact test to derive significance[69] or over- or underrepresentation under the assumption that the two variables are unrelated. A corresponding test for an increasing (or decreasing) enrichment substitutes the Fisher's noncentral hypergeometric distribution for the null model[70] in place of the centered hypergeometric distribution.

By assuming an evolutionary directed acyclic graph (not to be confused with the clonal tree graph) of groups that retains the degree of previous acquired pathway aberrations and introduces novel ones, a series of noncentral hypergeometric tests can be constructed to select a model among the candidate evolutionary graphs. Given the groups evolving (E), maintaining (M), adaptive (A) and their determined timing, the candidates are: E M A, E M > A, E > A M, E > A M > A, E > M A, E > M M > A, E > M E > A, E > M E > A M > A, where A > B represents an edge and A B no edge in the evolutionary graph.

Specifically, the maximum likelihood (ML) estimates of the noncentral hypergeometric models are first fit for all the partitions of the nodes of the evolutionary graph. In our setting, this involves the patient groups E, M, and A, giving the partitions EMA, E|MA, EM|A, EA|M, and E|M|A. Here, AB implies that the nodes A and B belong to the same subset of a partition and share the enrichment odds, while A|B implies two partitions where the odds can differ. Given a partition P with labeling $L_{:}$, and a set of odds ratios ω_k, one for the k:th subset P_k of the partition each, the likelihood is given by:

$$\Lambda_{P,\omega,j} = \prod_k \prod_{j \in P_k} f_{\text{fnc}}(a_{ij}, b_{ij}, c_{ij}, d_{ij} \vee \omega_k)$$

where $(a_{ij}, b_{ij}; c_{ij}, d_{ij})$ are the counts of the 2-by-2 crosstabulation regarding the i:th test (e.g. the i:th pathway) on the j:th node and f_{fnc} is the density of the noncentral hypergeometric distribution. In practice, the maximum likelihood estimate $\hat{\omega}_{ik}^{(P)}$ for each test and partition can be found numerically using sectioning.

The corresponding ML fits constrained by an evolutionary graph can be acquired from the above fits, namely, they occur at the ML estimates of one of the partitions whose ML estimates satisfies the evolutionary enrichment constraints as discussed above. Specifically, we write the likelihood of an evolutionary graph G as:

$$\Lambda_{G,\omega} = \prod_i \max_{P \text{ s.t. } \hat{\omega}_{i,:}^{(P)} \text{ feasible in } G} \Lambda_{P,\hat{\omega}_{i,:}^{(P)},i}$$

where a set of parameters ω are feasible if $(\omega_{i,L_p} \geq 1 \wedge \omega_{i,L_q} \geq \omega_{i,L_p}) \vee (\omega_{i,L_p} \leq 1 \wedge \omega_{i,L_q} \leq \omega_{i,L_p})$ for all edges from p to q in G, that is increased or decreased odds become no less extreme along the evolutionary graph. The appropriate evolutionary graph is selected using a series of likelihood ratio test comparing for nested evolutionary candidate graphs (cf. Figure S3A) with degrees of freedom equal to the total number of required partitions. The disconnected graph "E M A", where the groups are independent with no constraints, is always a putative candidate (cf. Figure S3), however, more constrained models should be favored if the evidence permits.

In a similar fashion, a likelihood ratio can be used to assess whether a specific pathway increases or decreases in enrichment along an edge from the p:th to q:th node of the selected evolutionary graph by comparing the model $\widehat{G}$ with one with the appropriate edge deleted $\widehat{G}(p,q)$. The pathway edge enrichment tests for the selected model E > M E > A M > A, with one of the edges E > M, E > A, or M > A deleted tabulated in Table S10.

RNA–seq data analyses

The preprocessing and subsequent decomposition of 317 RNA-seq diagnostic samples was performed as described in.[25] Pathway enrichment scores in sample and patient level for six unique signaling cascades were computed with 20,000 permutations using R package fgsea. First, we ranked each gene across all the samples, and normalized the rank values to be in [0,1]. Then, for each sample, we ordered the rank values inside out and in a decreasing order as inputs in fgsea analysis. The enrichment scores and adjusted p values are obtained for each individual sample. To get the patient level enrichment scores, we summed up the RNA expression data for each patient (with multiple samples), and then used that as the input for the ranking and ordering procedure. The same fgsea analysis was conducted in patient level and the corresponding enrichment scores and adjusted p values were obtained here as well. Cell type composition was quantified using PRISM.[25] The downstream statistical analyses of the enrichment scores and cell type abundances (excluding samples from ascites) were performed using ANOVA, and statistical significance of results was defined using a threshold of p value < 0.05.

Morphological analysis

Digitalized hemotoxylin and eosin (H&E) stained slides from archived samples collected for routine histopathological diagnostics were collected from Auria Biobank and used to discover growth pattern differences between the evolutionary states. All PDS patients from discovery cohort with representative images available were used, and the set was completed with patients from validation cohort, selecting especially low-fibroblast cases which were not included in all states in the original set (Table S6).

All scanned slides were evaluated by a gyneacological pathologist without knowledge of evolutionary state stratification or RNA cell type decomposition quantification. The following architectural patterns per slide were noted: solid, cribriform/pseudoendometrioid, transitional cell carcinoma-like, expansive/confluent papillary growth with pushing-border type invasion, true micropapillary, infiltrative papillary, infiltrative glandular/micropapillary, and infiltrative nested growth. Later, solid, cribriform/pseudoendometrioid and transitional patterns were grouped to SET-pattern, and infiltrative papillary and glandular/micropapillary patterns to infiltrative adenopapillary pattern. The most common (predominant pattern) was reported, as well as secondary, tertiary and minority patterns.

Organoid drug response in cytotoxicity assay

Organoid seeding and drug treatment

Growth medium was removed from BME-2-organoid cultures and each well was washed once with 1 ml PBS. Then, 2 ml TrypLE™ Express was added to each well and BME-2-organoid spheres were scraped from the well bottom. BME-2 sphere structure was deformed by pipetting 4-5 times in TrypLE™ Express after which the plate was incubated for 15 min at 37°C. The BME-2 gel structure was dissolved, and the organoid suspension was collected in 15 ml conical tubes (Avantor, #89039-668), and centrifuged at 240 RCF for 5 min. The supernatant was discarded, and the pellet of organoids was resuspended in 1:1 cold mixture of BME-2 (7 ng/ml) and PBS. Next, 10 μl of this suspension was seeded to each well of a pre-cooled 384-well Falcon plate (Falcon, #353962). Depending on

organoid growth rate, organoids were seeded in appropriate numbers to be 70% confluent at the time of drug treatment. The plate was incubated for 30 min at 37°C to ensure complete BME-2 solidification. Then, 40 μl of Plasmax™ (Ximbio, #156371) supplemented with 100 μg/mL Primocin (InvivoGen, #ant-562 pm-1), 10 mM HEPES (Gibco, #15630080), 1:100-diluted 100x GlutaMAX (Gibco, #35050061), 1:50-dilution of 50 x B-27 Supplement minus vitamin A (Thermo Fischer Scientific, #12587010), 0.5 μM SB202190 (MedChemExpress, #HY-10295), 0.5 μM A83-01 (Sigma, #SML0788),10 ng/ml Recombinant Human FGF-10 (Peprotech, #100-26), 10 ng/ml recombinant human FGF-4 (Peprotech, #100-31), 100 nM β-Estradiol (Sigma, #E2758) and 0.06 μM 2-hydroxybutyric acid was added to the BME-2-organoid spheres.[71] After 3-4 days in culture, organoids were treated with alpelisib (Selleck Chemicals, #S2814), idelalisib (MedChem Express, #HY-13026) and umbralisib (MedChem Express, #HY-12279) in the indicated final concentrations (10, 50 and 100 μM), along with vehicle/negative control DMSO (Avantor, #AMREN182) and 10 μM positive control bortezomib (Selleck Chemicals, #PS-341). Each experimental condition was performed in quadruplicates. 72 h following the drug treatments, organoids were stained by incubating with Hoechst 33342 Trihydrochloride, Trihydrate (Merck, #B2261) and propidium iodide (PI, Sigma-Aldrich, #P4864) for 1 h at 37°C for the detection of the whole number of cells (Nuclei) and dead cells respectively.

Image acquisition

High-throughput image acquisition of organoid microplate (Falcon, #353962) was carried out using ImageXpress Confocal HT.ai with 10x objective. Nuclei (Hoechst 33342) were identified at the DAPI channel and dead cells (PI) at the Texas Red channel. Two frames were scanned per well and 5-7 z-stacks images with 10 μm step size were acquired per site generating a complete 2D projection image of the 3D analyzed BME-2-organoid volume. DAPI channel was used to adjust the focus, and the optimal exposure for Texas Red was set avoiding image saturation. The same settings were used throughout the scanning of the whole plate.

Image-based analysis pipeline and statistical analysis

Image-based analysis and quantification of the high-throughput scanning was performed in an automatic and unbiased way via MetaXpress analysis software (Molecular Devices). In the custom module workflow, all nuclei were identified as individual round objects as depicted at the DAPI image indicating the total number of cells (both live and dead cells). Similarly, individual round objects found in the Texas Red image that overlapped with the nuclei were marked as the total number of dead cells. The percentage of dead cells out of total number of cells was calculated per condition. Then, the death index was estimated by normalization to the negative (set up as 100% viability) and positive (set up as 0% viability) controls. Data visualization was performed via GraphPad Prism and values were plotted in bar charts and represented as mean±SEM. Each bar represented pooled data from three different biological experiments where each experimental condition was repeated in four replicates. Statistical significance was calculated via one-way ANOVA combined with Dunnett's multiple comparisons to the negative control and p values were calculated. In all cases, $p > 0.05$, *: $p < 0.05$, **: $p < 0.01$, ***: $p < 0.001$, and ****: $p < 0.0001$.

Organoid drug response in proliferation assay

Organoid seeding and drug treatment

Growth medium was removed from BME-2-organoid cultures and each well was washed once with 1 ml PBS. Then, 2 ml TrypLE™ Express was added to each well and BME-2-organoid spheres were scraped from the well bottom. BME-2 sphere structure was deformed by pipetting 4-5 times in TrypLE™ Express and then, the plate was incubated for 15 min at 37°C. The BME-2 gel structure was dissolved, and the organoid suspension was collected in 15 ml conical tubes (Avantor, #89039-668), and centrifuged at 240 RCF for 5 min. The supernatant was discarded, and the pellet of organoids was resuspended in 1:1 cold mixture of BME-2 (7 ng/ml) and PBS. Next, 20 μl of this suspension was seeded to each well of a 96-well Screenstar microplate (Greiner, #655866). Organoids were seeded in appropriate numbers to be 70% confluent at the time of drug treatment. The plate was incubated for 30 min at 37°C to ensure complete BME-2 solidification. BME-2-embeded organoids were covered with 100 μl of experimental medium; Plasmax™ (Ximbio, #156371) supplemented with 100 μg/mL Primocin (InvivoGen, #ant-562 pm-1), 10 mM HEPES (Gibco, #15630080), 1:100-diluted 100x GlutaMAX (Gibco, #35050061), 1:50-dilution of 50 x B-27 Supplement minus vitamin A (Thermo Fischer Scientific, #12587010), 0.5 μM SB202190 (MedChemExpress, #HY-10295), 0.5 μM A83-01 (Sigma, #SML0788),10 ng/ml Recombinant Human FGF-10 (Peprotech, #100-26), 10 ng/ml recombinant human FGF-4 (Peprotech, #100-31), 100 nM β-Estradiol (Sigma, #E2758), and 0.06 μM 2-hydroxybutyric acid.

Organoids were cultured for 3-4 days, before treatment with 50 μM alpelisib, idelalisib, umbralisib, and vehicle/negative control DMSO (Avantor, #AMREN182). Each experimental condition was performed in triplicates. Organoids were incubated with the drugs for 48 h.

Fixation, quenching, blocking and antibody penetration

Direct fixation of embedded organoids was achieved with the addition of preheated 4% paraformaldehyde (PFA; Alfa Aesar, #043368) for 15 min. PFA was washed off three times with PBS for 10 minutes. Subsequently, organoids were quenched with 0.2 μM glycine in PBS for 15 min, permeabilized with 0,5% Triton X100 in PBS for another 15 min, and then incubated in blocking buffer 0,1% Triton X100, 0,05 % Tween, 1%BSA in PBS for 1 h. Between each step, organoids were thoroughly washed three times with 3% BSA in PBS for 10 min. Finally, organoids were incubated with primary antibodies against Ki67 (1:150) and E-cadherin (1:250) diluted in the blocking buffer overnight at 4 °C under mild agitation.

Next day, organoids were washed three times with the blocking buffer for 10 minutes. Then, they were incubated with secondary antibodies donkey anti-mouse IgG (H+L) (Alexa Fluor 594) and depending on the primary antibody either donkey anti-rabbit IgG (H+L) (Alexa Fluor 488) or goat anti-rat IgG (H+L) (Alexa Fluor 488) (1:1000) diluted in the blocking buffer for 2 h. During the incubation period

with the secondary antibodies, samples were protected from light. Organoids were then washed three times with blocking buffer and one time with PBS for 10 minutes. Nuclear DNA staining was achieved by incubation with Hoechst 33258 diluted in PBS (1:1000) for 30 min. Three additional washes with PBS for 10 minutes were performed. All steps were performed at RT under mild agitation unless stated otherwise. Finally, the embedded organoids were covered with PBS prior to image acquisition.

Image acquisition

High-throughput image acquisition of immunostained organoids in Screenstar microplates (Greiner, #655866) was carried out with ImageXpress Confocal HT.ai using 40x water immersion objective. Nuclei (Hoechst 33258) were identified at the DAPI channel, Ki67 protein structure in the Texas Red, and the marker of the cell membrane E-cadherin in the FITC channel. 5 sites were scanned per well and approximately 20-25 z-stack images with 1 μm step size in between were acquired per site generating a complete 3D BME-2-embedded organoid structure. DAPI channel was used to adjust the focus and optimal exposures of the other channels were set avoiding image saturation. The same settings were used throughout the scanning of the whole plate.

Image-based pipeline and statistical analysis

Image-based analyses and quantifications of the high-throughput scanning images were performed in an automatic and unbiased way with MetaXpress analysis software (Molecular Devices). In the custom module workflow, nuclei were identified in the DAPI image of every z-stack of a site and objects that overlapped in between the z-stacks were counted only once. Cell cytoplasm was identified in the FITC image indicated by E-cadherin detection and together with the cell nuclei formed the mask of the organoid structures.

The Texas Red image was analyzed by applying a filter mask where the lowest possible intensity of Ki67 signal was set. All objects with intensity higher than the threshold were identified as Ki67 signal. Then, the Ki67 signal that overlapped with the identified nuclei was marked as positive counts. In the analysis output, the organoid mask was used to identify all the cell nuclei, which were then marked positive or negative for the Ki67.

The percentage of Ki67 positive nuclei out of the total number of nuclei was calculated per condition by normalization to the negative control (set up as 100% proliferation). Data visualization was performed via GraphPad Prism and values were plotted in bar charts and represented as mean±SEM. Each bar represents pooled data from three different biological experiments where each experimental condition was repeated in triplicates. Statistical significance was performed via one-way ANOVA combined with Dunnett's multiple comparisons to the negative control and p values were calculated. In all cases, $p > 0.05$, *: $p < 0.05$, **: $p < 0.01$, ***: $p < 0.001$, and ****: $p < 0.0001$.

QUANTIFICATION AND STATISTICAL ANALYSIS

Statistical analyses were performed in R (versions 3 and 4), Matlab (2012b) and Prism (GraphPad). Prism was used for organoid data after automatic quantification of the cells through MetaXpress (Molecular Devices). Group comparisons were performed with ANOVA without test of normality, in Prism for organoids and in R for other analyses. Kaplan-Meier analysis was performed with R package survival (v.3.1-12). For clustering of clonal complexity and divergence, weighted K-means was used. Statistical tests related to figures are indicated in the figure legends. Number of individuals or samples in each test are explained in the Results.

Pathway enrichment analyses were performed patient-wise with R packages ReactomePA (v1.38.0) for mutations and fgsea (v1.12.0) for expression data. Nested pathway analysis and clonal complexity and divergence estimations were developed for this paper.

Further statistical details of the analyses are defined in the corresponding method sections of the STAR Methods.

ADDITIONAL RESOURCES

This study is a part of DECIDER trial, ClinicalTrials.gov Identifier: NCT04846933, accessed at https://clinicaltrials.gov/ct2/show/NCT04846933.

The visualization of genomic data was performed using GenomeSpy (https://genomespy.app/) and is available at https://csbi.ltdk.helsinki.fi/p/lahtinen_et_al_2023/.